1 **Cardiolipin deficiency disrupts CoQ-complex III interface in steatohepatitis**

2

3 Marisa J. Brothwell,[1,2] Guoshen Cao,[1,3] J. Alan Maschek,[1,2,4] Annelise M. Poss,[1,2] Alek D.

4 Peterlin,[1,2] Liping Wang,[1,2] Talia B. Baker,[5,6] Justin L. Shahtout,[1,7] Piyarat Siripoksup,[1,7] Quentinn

5 J. Pearce,[4] Jordan M. Johnson,[1,2] Fabian M. Finger,[8,9] Alexandre Prola,[10] Sarah A. Pellizzari,[3,11]

6 Gillian L. Hale,[5,11] Allison M. Manuel,[4] Shinya Watanabe,[1,2] Edwin R. Miranda,[1,2,12] Kajsa E.

7 Affolter,[5,10] Trevor S. Tippetts,[1,2] Linda S. Nikolova,[13] Ran Hee Choi,[1,2,12] Stephen T. Decker,[1,2,12]

8 Mallikarjun Patil,[1,2,12] J. Leon Catrow,[4] William L. Holland,[1,2,3,12] Sara M. Nowinski,[14] Daniel S.

9 Lark,[15,16] Kelsey H. Fisher-Wellman,[17] Patrice N. Mimche,[18] Kimberley J. Evason,[5,11] James E.

10 Cox,[1,3,4] Scott A. Summers,[1,2,3,5,12] Zach Gerhart-Hines,[8,9] Katsuhiko Funai[1,2,3,5,7,12]*

11

12 [1]Diabetes & Metabolism Research Center; University of Utah; Salt Lake City, UT; USA.

13 [2]Department of Nutrition and Integrative Physiology; University of Utah; Salt Lake City, UT;

14 USA.

15 [3]Department of Biochemistry; University of Utah; Salt Lake City, UT; USA.

16 [4]Metabolomics Core Research Facility; University of Utah; Salt Lake City, UT; USA.

17 [5]Huntsman Cancer Institute; University of Utah, Salt Lake City, UT; USA.

18 [6]Division of Transplantation and Advanced Hepatobiliary Surgery, Department of Surgery;

19 University of Utah; Salt Lake City, UT; USA.

20 [7]Department of Physical Therapy and Athletic Training; University of Utah; Salt Lake City, UT;

21 USA.

22 [8]Novo Nordisk Foundation Center for Basic Metabolic Research; University of Copenhagen;

23 Copenhagen; DK.

24 [9]Center for Adipocyte Signaling (ADIPOSIGN); University of Southern Denmark; Odense; DK.

25 [10]Laboratory of Fundamental and Applied Bioenergetics; University of Grenoble Alpes, Inserm

26 U1055; Grenoble; FR.

27   [11]Department of Pathology; University of Utah; Salt Lake City, UT; USA.

28   [12]Molecular Medicine Program; University of Utah; Salt Lake City, UT; USA.

29   [13]Electron Microscopy Core Facility; University of Utah; Salt Lake City, UT; USA.

30   [14]Department of Metabolism and Nutritional Programming; Van Andel Institute; Grand Rapids,

31   MI; USA.

32   [15]College of Health and Human Sciences; Colorado State University; Fort Collins, CO; USA.

33   [16]Columbine Health Systems Center for Healthy Aging; Colorado State University; Fort Collins,

34   CO; USA

35   [17]Department of Cancer Biology, Wake Forest University School of Medicine; Atrium Health

36   Wake Forest Baptist Comprehensive Cancer Center; Winston-Salem, NC; USA.

37   [18]Departments of Dermatology and Medicine; Division of Gastroenterology and Hepatology,

38   Indiana University School of Medicine; Indianapolis, IN; USA.

39

40   *Lead Contact

41   Correspondence:

42   Katsuhiko Funai, Ph.D.

43   kfunai@health.utah.edu

44

Abstract

Metabolic dysfunction-associated steatotic liver disease (MASLD) is a progressive disorder marked by lipid accumulation, leading to steatohepatitis (MASH). A key feature of the transition to MASH involves oxidative stress resulting from defects in mitochondrial oxidative phosphorylation (OXPHOS). Here, we show that pathological alterations in the lipid composition of the inner mitochondrial membrane (IMM) directly instigate electron transfer inefficiency to promote oxidative stress. Specifically, mitochondrial cardiolipin (CL) was downregulated with MASLD/MASH in mice and in humans. Hepatocyte-specific CL synthase knockout (CLS-LKO) led to spontaneous and robust MASH with extensive steatotic and fibrotic phenotype. Loss of CL paradoxically increased mitochondrial respiratory capacity but also reduced the formation of I+III$_2$+IV$_1$ respiratory supercomplex and interfered with the ability of coenzyme Q (CoQ) to transfer electrons to complex III. In turn, the bottleneck at complex III promoted electron leak primarily at site III$_{Q0}$ as well as other upstream sites in the electron transport chain. Thus, reduction in mitochondrial CL promotes oxidative stress and contributes to pathogenesis of MASH.

Main

Metabolic dysfunction-associated steatotic liver disease (MASLD) is a growing global health

concern with an increasing prevalence that parallels the rise in obesity.[1] In the United States,

annual medical costs related to MASLD exceed $103 billion.[2] A large portion of patients with

MASLD only exhibit steatosis, a silent and relatively benign early stage characterized by lipid

accumulation in hepatocytes without hepatocellular inflammation.[3] Steatosis can then progress

to metabolic dysfunction-associated steatohepatitis (MASH), determined by hepatocyte injury

and tissue fibrosis.[4] MASH is the last stage of MASLD that may be reversible, making

intervention at this stage particularly important.[3,5] Although extensive clinical and basic research

have been conducted in this field, the underlying mechanisms by which fatty liver transitions to

MASH remain poorly understood.[6-8]

A defect in mitochondrial function is considered one of the hallmarks of MASLD progression in

both mice and humans.[9-12] MASLD is initially associated with an increase in mitochondrial

respiratory capacity, followed by a subsequent impairment in oxidative phosphorylation

(OXPHOS), and increased production of mitochondrial reactive oxygen species (ROS).[11,13]

Mitochondrial ROS is thought to be caused by an inefficient electron transport chain (ETC) that

increases the propensity for electron leak. However, the mechanisms by which mitochondrial

electron leak promotes MASLD are unknown.

Cardiolipin (CL) is a phospholipid with four acyl chains conjugated to two phosphatidylglycerol

moieties linked by another glycerol molecule.[14] CL resides almost exclusively in the inner

mitochondrial membrane (IMM), constituting approximately 15–20% of the mitochondrial

phospholipids.[15] CL is synthesized by the condensation of phosphatidylglycerol (PG) and

cytidine diphosphate-diacylglycerol (CDP-DAG) at the IMM via the enzyme cardiolipin synthase

(CLS).[16,17] Structural studies indicate that CL is essential for the activities of OXPHOS

87 enzymes.[18-22] In non-hepatocytes, decreased CL leads to compromised oxidative capacity,[23,24]

88 impaired membrane potential,[25] and altered cristae morphology.[26] In particular, low CL is

89 associated with increased H_2O_2 production.[27,28]

90

91 In this manuscript, we set out to examine the changes in liver mitochondrial lipidome induced by

92 MASH. In both mice and in humans, mitochondrial CL was downregulated in livers with

93 MASLD/MASH compared to healthy controls. We then performed a targeted deletion of CLS in

94 hepatocytes and studied its effects on liver, mitochondrial bioenergetics, and potential

95 mechanisms that drive these changes.

96

97 **Results**

98 **Mitochondrial cardiolipin levels are decreased in mouse models of MASLD/MASH**

99 Previous research from our lab in non-hepatocytes indicated that mitochondrial phospholipid

100 composition affects OXPHOS electron transfer efficiency to alter electron leak.[15,29,30] MASLD

101 has been shown to alter the total cellular lipidome in liver.[31] However, MASLD may also

102 influence mitochondrial content in the hepatocytes, making it difficult to discern whether these

103 are changes in the lipid composition of mitochondrial membranes and/or changes in cellular

104 mitochondrial density. Thus, we performed liquid chromatography-tandem mass spectrometry

105 (LC-MS/MS) lipidomics specifically on mitochondria isolated from human liver samples with or

106 without MASH. Samples from patients undergoing liver transplant or resection due to end-stage

107 MASH (Fig. 1a, and Extended Data Table 1) were compared to samples from patients without

108 MASH, undergoing resection for benign liver tumors or metastases (Fig. 1b). Strikingly,

109 mitochondrial CL levels were reduced, primarily due to a decrease in tetralinoleoyl CL (Fig. 1c),

110 commonly thought as the mature and functional form of CL. Additionally, levels of mitochondrial

111 PG, an essential precursor to CL production, were also reduced, suggesting a disruption in CL

112 biosynthesis (Fig. 1d-e).

113

114 We next performed lipidomic analyses on four distinct mouse models of MASLD/MASH (Fig. 1f-

115 q). These included: 1) mice given a Western high-fat diet (HFD, Envigo TD.88137) or standard

116 chow diet for 16 weeks (Fig. 1f), 2) ob/ob mice or their wildtype littermates at 20 weeks of age

117 (Fig. 1g), 3) mice given the Gubra Amylin NASH diet for 30 weeks (GAN, Research Diets

118 D09100310) or standard chow (Fig. 1h), 4) mice injected with carbon tetrachloride (CCl_4) or

119 vehicle (corn oil) for 6 weeks (Fig. 1i). Importantly, none of these interventions appear to alter

120 the protein abundances of OXPHOS subunits or citrate synthase (Fig. 1j-m), suggesting that

121 these interventions did not alter mitochondrial density in hepatocytes. Nevertheless, we

122 performed all mitochondrial lipidomic analyses by quantifying lipids per mg of mitochondrial

123 proteins. Each intervention appeared to alter different subsets of mitochondrial lipid classes

124 (Fig. 1n-q, and Extended Data Fig. 1 and 2), as seen with our previous studies in skeletal

125 muscle and brown adipose tissues.[29,30] We take these observations to mean that most

126 physiological interventions induce multiple systemic and local responses that are not

127 mechanistically directly related to the phenotype of interest (e.g., cold exposure or exercise can

128 increase food intake, obesity could affect locomotion and insulation, etc.). Although several

129 phospholipid classes were altered among the four models, strikingly, mitochondrial CL was

130 reduced in all four MASLD/MASH models (Fig. 1n-r). Furthermore, PG was significantly

131 increased in all MASLD/MASH models (Fig. 1n-r). These changes coincided with decreased

132 transcript levels for CLS (Fig. 1s-v). These observations further suggest that an insult in CL

133 synthesis may be a key factor to disrupting mitochondrial function in MASLD/MASH.

134

135 **Hepatocyte-specific deletion of cardiolipin synthase promotes MASH**

136 CL is thought to be exclusively synthesized in the IMM where CLS is localized. To study the role

137 of CL in hepatocytes, we generated mice with hepatocyte-specific knockout of CLS (CLS-LKO

138 for *CLS liver knockout*, driven by albumin-Cre) (Fig. 2a,b), which successfully decreased

139   mitochondrial CL levels (Fig. 2c, and Extended Data Fig. 3). Consistent with our previous

140   studies in non-hepatocytes, CLS deletion does not completely reduce CL levels to zero,

141   suggesting that CL generated in other tissues may be imported. Our results showed that

142   decreased levels of CL did not significantly impact body weight or composition (Fig. 2d,e) but

143   resulted in significantly less liver mass (Fig. 2f).

144

145   We sought to further characterize livers from control and CLS-LKO mice. Histological analyses

146   revealed that CLS deletion was sufficient to promote steatosis (Fig. 2g) and fibrosis (Fig. 2h) in

147   standard chow-fed and high-fat fed conditions (Extended Data Fig. 4a,b). To more

148   comprehensively describe the effects of loss of hepatic CLS on gene expression, we performed

149   RNA sequencing on these livers. CLS deletion increased the expression of 713 genes and

150   decreased 1026 genes (Extended Data Fig. 4c). Pathway analyses revealed that many of the

151   signature changes that occur with MASLD/MASH also occurred with CLS deletion (Fig. 2i, and

152   Extended Data Fig. 4d). This MASLD/MASH phenotype in our CLS knockout model was further

153   confirmed with an elevation of the liver enzymes AST and ALT (Fig. 2j,k) as well as increased

154   mRNA levels of inflammatory markers (Fig. 2l). We then proceeded to confirm these data by

155   further phenotyping liver tissues from control and CLS-LKO mice.

156

157   In steatohepatitis, immune cell populations in the liver become altered to activate pathological

158   immune response.[32] Flow cytometry on livers from control and CLS-LKO mice indicated that the

159   loss of CL promotes a robust classic immune response found in MASH (Fig. 2m). cDC2 cells

160   are a broad subset of dendritic cells with specific surface markers (e.g., CD11b, CD172a) that

161   allow them to be distinguished from other dendritic cell populations.[33] This broad population of

162   dendritic cells was not different between control and CLS-LKO mice (Fig. 2n). Notably, there

163   was a marked reduction in the Kupffer cell population (Fig. 2o) - traditionally involved in

164   maintaining liver homeostasis whose dysfunction can lead to dysregulated immune response.[34]

165   This reduction appears to be counterbalanced by a concomitant increase in Ly6C^{hi} population,

166   which are known to typically go on to become inflammatory monocytes (Fig. 2m,p). The

167   replacement of Kupffer cells with other inflammatory cell populations suggests a shift towards a

168   more pro-inflammatory environment, which may exacerbate liver injury and promote fibrosis.

169   Nonetheless, the MHC-II cell population and neutrophils were not increased (Fig. 2q,r) with

170   neutrophils actually decreased (Fig. 2r). The cDC1 cell population was not different, which is

171   traditionally elevated in response to cytotoxic T cells and might not be directly related to liver

172   fibrosis.[35] Together, these findings suggest that even on a chow diet, CLS-deficient livers exhibit

173   inflammatory cell infiltration, a hallmark often associated with early signs of MASH.

174

175   **CLS deletion promotes fatty liver but increases mitochondrial respiratory capacity**

176   Hepatocyte lipid accumulation may suggest defects in substrate handling, which is often

177   manifested in systemic substrate handling. Indeed, CLS deletion modestly reduced glucose or

178   pyruvate handling, even in chow-fed conditions (Fig. 3a-d). Lipid accumulation in hepatocytes

179   can occur due to an increase in lipogenesis, a decrease in VLDL secretion, or a decrease in β-

180   oxidation. However, mRNA levels for lipogenesis genes trended lower (not higher), and mostly

181   unchanged for VLDL secretion or β-oxidation (Fig. 3e, and Extended Data Fig. 5a). Circulating

182   triglycerides were not lower in CLS-LKO mice compared to control mice (Extended Data Figure

183   5b).

184

185   MASLD is known to be associated with reduced mitochondrial oxidative capacity, and such an

186   effect may also occur with CL deficiency to induce lipid accumulation. Indeed, mRNA levels of

187   several genes in the ETC were downregulated with CLS deletion, particularly those associated

188   with structural components of the ETC complexes and the electron carrier CoQ (Fig. 3f). Given

189   that CL is located in the IMM where it binds to enzymes involved in OXPHOS,[36-39] we reasoned

190   that the loss of CL could reduce mitochondrial oxidative capacity to promote steatosis.

191 Consistent with subcellular localization of CL, CLS deletion resulted in mitochondria with

192 disorganized membrane structures and poorly developed cristae (Fig. 3g). However,

193 mitochondrial density quantified with western blots for respiratory complex subunits and citrate

194 synthase (Fig. 3h), as well as mtDNA/nucDNA (Fig. 3i), showed no differences in livers from

195 control and CLS-LKO mice. We thus speculated that CL lowers respiratory capacity not by

196 reducing the total number of mitochondria or OXPHOS respirasomes, but by reducing the

197 activity of respiratory enzymes. To our surprise, CLS deletion increased, rather than decreased,

198 mitochondrial respiration (JO_2), as measured by high-resolution Oroboros respirometry (Fig. 3j),

199 using both with Krebs cycle substrates (Fig. 3k) as well as fatty acyl substrates (Fig. 3l), to a

200 similar degree. Importantly, these changes occurred in the absence of differences in OXPHOS

201 subunit abundance per unit of mitochondria (Fig. 3m), ruling out the possibility that changes in

202 the abundance of respiratory enzymes to contribute to change in respiration. A caveat to these

203 findings is that CLS deletion promotes reduction in respiratory capacity after HFD-feeding

204 (Extended Data Fig. 5c,d). However, CLS-LKO mice are steatotic in standard chow-fed

205 condition, indicating that reduced mitochondrial fatty acid oxidation cannot be the cause of

206 steatosis at baseline. The transient increase in respiration followed by its subsequent decrease

207 is reminiscent of what is thought to occur with liver's mitochondrial respiration over the course of

208 MASLD progression.[40]

209

210 High-resolution respirometry experiments were performed in isolated mitochondria from

211 hepatocytes by providing exogenous supraphysiological concentrations of substrates. While

212 these assays provide robust measurements of respiratory capacity (the potential of

213 mitochondria), they do not necessarily reflect their endogenous activity. To address this point,

214 we performed stable isotope tracing experiments using uniformly labeled ^{13}C-palmitate (Fig.

215 4a)[41] in murine hepa1-6 cells without (scrambled shRNA or shSC) or with CLS knockdown

216 (shRNA targeting CLS or shCLS). Surprisingly, but consistent with the JO_2 data, CLS deletion

217 increased, not decreased, the incorporation of palmitate into TCA intermediates (Fig. 4b-d). We

218 also performed a similar tracing experiment using uniformly labeled ^{13}C-glucose (Fig. 4e-j, and

219 Extended Data Fig. 5e-i) and observed increased labeling towards pyruvate (Fig. 4e,f), reduced

220 labeling towards lactate and alanine (Fig. 4g, and Extended Data Fig. 5h), and normal labeling

221 towards TCA intermediates except for reduced labeling towards succinate (Fig. 4h-j, and

222 Extended Data Fig. 5i-m). Overall, despite the altered substrate incorporation, a decrease in

223 TCA flux does not appear to account for the steatotic phenotype observed with CLS deletion.

224

225 **Low hepatic CL paradoxically increases mitochondrial respiratory capacity and promotes**

226 **electron leak**

227 Oxidative stress is thought to play a critical role in the transition from MASLD to MASH, wherein

228 sustained metabolic insult leads to hepatocellular injury and collagen deposition resulting in

229 fibrosis.[7] CLS deletion promotes liver fibrosis in standard chow-fed condition (Fig. 5a and Fig.

230 2h) and in HFD-fed condition (Extended Data Fig. 4b) that coincided with increased mRNA

231 levels for fibrosis (Fig. 5b and 2i). Tissue fibrosis is often triggered by apoptosis, and CLS

232 deletion appeared to activate the caspase pathway (Fig. 5c,d). How does deletion of CLS, a

233 mitochondrial enzyme that produces lipids for IMM, activate apoptosis? Cytochrome c is an

234 electron carrier that resides in IMM, which shuttles electrons between complexes III and IV.[42]

235 Under normal physiological conditions, cytochrome c is anchored to the IMM by its binding to

236 cardiolipin.[39] During the initiation of intrinsic apoptosis, CL can undergo oxidation and

237 redistribution from the IMM to the outer membrane space (OMM). CL oxidation weakens its

238 binding affinity for cytochrome c, releasing it from the IMM and into the OMM where it signals

239 apoptosis.[13] However, neither mitochondrial nor cytosolic cytochrome c abundance appeared to

240 be influenced by CLS deletion (Fig. 5e,f, and Extended Data Fig. 6a,b).

241

242   Mitochondrial ROS has been implicated in apoptosis and fibrosis with MASLD.[43-45] Using high-

243   resolution fluorometry in combination with high-resolution respirometry, we quantified electron

244   leak from liver mitochondria with the assumption that almost all electrons that leak react with

245   molecular O_2 to produce O_2^-. Using recombinant superoxide dismutase, we ensure that all O_2^-

246   produced is converted into H_2O_2, which was quantified with the AmplexRed fluorophore.[46] There

247   were striking increases in mitochondrial electron leak in CLS-LKO mice compared to control

248   mice on both standard chow (Fig. 5g) and high-fat diet (Extended Data Fig. 6c). It is noteworthy

249   that endogenous antioxidant pathways were insufficient to completely suppress oxidative stress

250   induced by CLS deletion (H_2O_2 emission shown in the 1st and 2nd bars in Fig. 5g, and Extended

251   Data Fig. 6c). We also confirmed that JH_2O_2/JO_2 was elevated with CLS knockdown in

252   mitochondria from murine hepa1-6 cell line (Extended Data Fig. 6d) suggesting that low CL

253   induces oxidative stress in a cell-autonomous manner.

254

255   While unknown, CLS may possess an enzymatic activity independent of CL synthesis that may

256   contribute to electron leak. To more conclusively show that the loss of mitochondrial CL

257   contributes to oxidative stress, we supplied exogenous CL to isolated mitochondria by fusing

258   them with small unilamellar vesicles (SUVs) (Fig. 5h).[47] Isolated mitochondria from control and

259   CLS-LKO mice were fused with SUVs containing either CL or phosphatidylcholine (PC) (Fig. 5i,

260   and Extended Data Fig. 6e). Remarkably, reintroducing CL to mitochondria from CLS-LKO mice

261   reduced H_2O_2 production back to baseline, whereas PC had no effect. Thus, loss of CL drives

262   the increased mitochondrial leak observed with CLS deletion.

263

264   **Loss of CL attenuates coenzyme Q interface with complex III**

265   How does the loss of CL promote electron leak? We first addressed whether CL influences the

266   formations of respiratory supercomplexes. Respiratory supercomplexes exist in several

267   combinations of multimers of Complex I, III, IV, and V and are thought to form either transiently

268   or stably to improve electron transfer efficiency.[48,49] CL may play an essential role in the stability

269   of ETC supercomplexes.[50,51] Using blue native polyacrylamide gel electrophoresis , we

270   investigated supercomplex assembly in isolated hepatic mitochondria from control and CLS-

271   LKO mice (Fig. 6). When probing indiscriminately for all supercomplexes, there were many

272   bands whose intensity were influenced by CLS deletion (Fig. 6a). In particular, $I+III_2+IV_1$

273   supercomplex appeared to be substantially and consistently reduced in samples from CLS-LKO

274   mice compared to control. To gain a more granular and definitive picture on the influence of

275   CLS deletion on individual supercomplexes, we quantified supercomplexes using subunit-

276   specific western blotting (Fig. 6b-m). Strikingly, CLS deletion substantially reduced the

277   abundance of $I+III_2+IV_1$ supercomplex when probing for UQCRSF1/complex III (Fig. 6h,i), while

278   increasing the abundances for CIII singlet and CIV singlet (Fig. 6j,k), as well as trends for

279   increase in CI singlet (Fig. 6b-e). These findings suggest that loss of CL reduces $I+III_2+IV_1$

280   supercomplex assembly to attenuate electron flux through these complexes, promoting electron

281   leak.

282

283   To better understand how low CL promotes inefficient electron transfer, we quantified electron

284   leak at four specific sites of the ETC: 1) quinone-binding site in complex I (I_Q), 2) flavin-

285   containing site in complex I (I_F), 3) succinate-dehydrogenase-associated site in complex II (II_F),

286   and 4) the ubiquinol oxidation site in complex (III_{Qo}) Fig. 7a). Electron leak at each of these sites

287   can be quantified separately using substrates and inhibitors that restrict electron flow specific to

288   these sites (Fig. 7b-e). Among complex I, III, and IV (the components of $I+III_2+IV_1$

289   supercomplex), CLS deletion robustly increased electron leak at site III_{Qo} (Fig. 7e). In addition,

290   electron leak either increased or trended to increase at all other upstream sites (Fig. 7b-d).

291   These findings raise a possibility that inefficient electron transfer at complex III bottlenecks the

292   ETC electron flow to increase electron leak at these sites.

293

294   We further examined the possibility that complex III is the primary site of defect induced by CLS

295   deletion, we studied the redox state of CoQ, a career that feeds electrons into complex III. It is

296   noteworthy that CoQ, like CL, is a lipid molecule (Fig. 7f), and we thought it was conceivable

297   that CL somehow interacts with CoQ to influence its electron transfer efficiency. Using redox

298   mass spectrometry, we measured CoQ levels in whole liver tissues from control and CLS-LKO

299   mice and found no difference in whole liver tissue CoQ levels (Extended Data Fig. 7a-i).

300   However, since CoQ may also be found outside of mitochondria, we performed CoQ redox

301   mass spectrometry in isolated mitochondria fractions of livers from control or CLS-LKO mice.

302   Indeed, oxidized CoQ levels were increased (Fig. 7g, and Extended Data Fig. 7j,l,n) in CLS-LKO

303   mice compared to their controls. In contrast, reduced forms of CoQ were not lower in CLS-LKO

304   mice compared to control mice (Fig. 7h, and Extended Data Fig. 7k,m,o). Thus, CLS deletion

305   does not appear to have a defect in converting oxidized CoQ into reduced CoQ (i.e., charging

306   CoQ with electrons by complex I and II). Rather, these data support the notion that the defect is

307   at complex III, as the normal level of reduced CoQ yielded greater oxidized CoQ.

308

309   To extrapolate these findings into humans, we went back to liver samples from patients

310   undergoing liver transplant or resection due to end-stage MASH (Fig. 1a) to quantify the

311   abundance of mitochondrial CoQ. MASH was associated with a striking ~40% reduction in the

312   abundance of mitochondrial CoQ (Fig. 7i) (tissue samples were not large enough to perform

313   CoQ redox mass spectrometry on mitochondria). A Pearson correlation analysis showed a

314   highly robust correlation between the abundances of mitochondrial CL and CoQ (Figure 7j, R^2 =

315   0.64), indicating that the variability in the abundance of CL explains 64% of the variability of the

316   abundance of CoQ. Based on our findings that CL is reduced with MASLD/MASH and that loss

317   of CL influences CoQ electron transfer efficiency, we interpret these findings to mean that loss

318   of CL destabilizes CoQ to increase its turnover.

319

Discussion

320

321 In hepatocytes, disruptions of mitochondrial bioenergetics lead to and exacerbate metabolic-

322 associated steatohepatitis.[52] CL, a key phospholipid in the inner mitochondrial membrane, plays

323 a critical role in mitochondrial energy metabolism.[23] In this manuscript, we examined the role of

324 CL in the pathogenesis of MASLD. In mice and in humans, MASLD/MASH coincided with a

325 reduction in mitochondrial CL levels. Hepatocyte-specific deletion of CLS was sufficient to

326 spontaneously induce MASH pathology, including steatosis and fibrosis, along with shift in

327 immune cell populations towards a more pro-inflammatory profile, all of which occurred in mice

328 given a standard chow diet. Paradoxically, high-resolution respirometry and stable isotope

329 experiments showed that CLS deletion promotes, instead of attenuates, mitochondrial oxidative

330 capacity in a fashion reminiscent of temporal changes that occur with mitochondrial

331 bioenergetics in human MASH.[40] Our principal finding on the role of hepatocyte CL in

332 bioenergetics is that its loss robustly increases electron leak, particularly at complex III. This

333 was likely due to: 1) direct interaction of CL with complex III, 2) lower abundance of $I+III_2+IV_1$

334 respiratory supercomplex, and 3) inability of complex III to efficiently accept electrons from CoQ.

335 In humans, mitochondrial CL and CoQ were co-downregulated in MASH patients compared to

336 healthy controls, with a strong correlation ($R^2 = 0.64$) between CL and CoQ. Together, these

337 results implicate CL as a key regulator of MASH progression, particularly through its effect on

338 the CoQ-complex III interface to promote oxidative stress.

339

340 How might CL regulate CoQ? CoQ is the main electron transporter between complex I/II and III.

341 CLS deletion in hepatocytes appeared to disrupt CoQ's ability to cycle between its oxidized and

342 reduced forms. There are several ways in which low CL might directly or indirectly influence

343 CoQ's redox state. The primary suspect is CL interacting with complex III, as eight or nine CL

344 molecules are tightly bound to complex III[38] and are thought to be essential to its function.[53]

345 While CL has been found to bind to other respiratory complexes, our data suggest that loss of

346   CL might disproportionately influence complex III. This is also supported by our findings that the

347   loss of CL reduced the formation of complex III-dependent supercomplex, without influencing

348   other supercomplexes. Reduced capacity for complex III to efficiently accept electrons from

349   CoQ might explain the increased electron leak at site III_{Q0} and increased level of oxidized CoQ.

350   Meanwhile, loss of CL also increased electron leak at complex I and II. CL has also been

351   implicated to bind to these complexes.[20,21,36] Thus, complex III dysfunction is perhaps unlikely to

352   entirely explain electron leaks at sites I_F, I_Q, and II_F, though we think that the majority of its effect

353   is due to the bottleneck created by the reduced ability of complex III to accept electrons.[54]

354   Conversely, complex I and II are unlikely to be the only primary sites of defect as such defects

355   probably will not promote electron leak at site III_{QO}. Moreover, CLS deletion did not have an

356   effect on the abundance of reduced CoQ despite there being greater abundance of oxidized

357   CoQ, suggesting that complex I/II do not have reduced ability to transfer electrons onto CoQ.

358   Another potential mechanism by which CL influences CoQ redox state is by CL directly

359   interacting with CoQ. As they are both lipid molecules in the IMM, low CL may reduce the lateral

360   diffusability of CoQ between respiratory complexes. Low CL might also indirectly influence CoQ

361   by contributing to changes in membrane properties, distribution of ETC in the cristae, and the

362   cristae architecture.[55] Finally, increased electron leak, regardless of their origin, could have a

363   feed-forward effect by which oxidative stress disrupts redox homeostasis in other components

364   of ETC.

365

366   MASH is a progressive liver disease characterized by lipid accumulation, inflammation, and

367   fibrosis in the liver.[56] The progression to MASH involves a complex interplay of metabolic stress,

368   mitochondrial defects, and immune responses that collectively promote hepatocellular injury.[57]

369   Our findings suggest that a low mitochondrial CL level directly induces key pathological features

370   of MASH, including steatosis, fibrosis, and immune cell infiltration, even in the absence of

371   dietary or environmental stressors, such as high-fat diet. When mice were fed a standard chow

372   diet, CLS-LKO mice were more prone to lipid droplet accumulation than control mice. This

373   phenotype was exacerbated when the mice were challenged with a high-fat diet. We primarily

374   interrogated the mitochondrial bioenergetics of standard chow-fed control or CLS-LKO mice. A

375   lower respiration rate would partially explain the lipid droplet accumulation, but to our surprise,

376   CLS deletion increased JO_2 regardless of substrates. Similarly, experiments using uniformly

377   labeled ^{13}C-palmitate or ^{13}C-glucose showed that CLS deletion promoted an overall increase in

378   the flux toward TCA intermediates, particularly for palmitate. CLS deletion did not appear to

379   increase de novo lipogenesis or reduce VLDL secretion. Thus, it is unclear what mechanisms

380   contribute to steatosis induced by CLS deletion.

381

382   Liver fibrosis is characterized by the accumulation of excess extracellular matrix components,

383   including type I collagen, which disrupts liver microcirculation and leads to injury.[55] Livers from

384   CLS-LKO mice exhibited more fibrosis compared to control mice, even on a standard chow diet,

385   which was worsened when fed a high-fat diet. Indeed, transcriptomic analyses revealed that

386   CLS deletion activates pathways for fibrosis and degeneration, with many of the collagen

387   isoforms upregulated. In the MASH liver, collagen deposition is accompanied by inflammatory

388   cell infiltrate promoting an overall inflammatory environment. Flow cytometry experiments

389   further confirmed that CLS deletion led to an increase in Ly6C^{hi} cell population, suggesting that

390   dying resident Kupffer cells are being replaced by Ly6C^{hi} monocytes in the livers of CLS-LKO

391   mice.[33]

392

393   Early in the MASLD disease progression, mitochondria adapt to the increased energy demands

394   by increasing their respiratory capacity. In the later stages of disease progression to MASH,

395   mitochondrial respiration diminishes.[58] This pattern was reminiscent of our observations in the

396   CLS-LKO mice. Livers from CLS-LKO mice fed a standard chow diet exhibited greater

397   respiratory capacity compared to that of control mice. Conversely, livers from CLS-LKO mice on

398   a high-fat diet exhibited lower respiratory capacity compared to that of control mice. We interpret

399   these findings to suggest that liver mitochondria in chow-fed CLS-LKO mice are more

400   representative of early stage of MASLD, while high-fat-diet fed CLS-LKO mice resemble later

401   stages of MASLD.

402

403   In non-hepatocytes, low CL levels have been linked to electron leak in the context of a

404   deficiency of the tafazzin gene, a CL transacylase, whose mutation promotes Barth

405   syndrome.[15,26,59,60] Paradoxically, we previously showed that CLS deletion in brown adipocytes

406   does not increase electron leak.[30] It is important to note that CLS deletion in our current or

407   previous study does not completely eliminate CL (likely due to an extracellular source). We do

408   not believe that CL is dispensable for efficient electron transfer in adipocytes. Rather, due to

409   unclear mechanisms, different cell types likely exhibit varying tolerances to low CL influencing

410   their bioenergetics, with brown adipocytes appearing more tolerant than hepatocytes.

411   Regardless, electron leak was elevated with CLS deletion in both standard chow and high-fat

412   diet-fed conditions. These observations mirror what has been shown in MASLD progression.[61]

413   The effect of CLS deletion on electron leak was due to reduced CL levels, as the reintroduction

414   of cardiolipin via SUVs completely rescued the electron leak.

415

416   CL is reported to be essential for the formation and stability of supercomplexes.[14,50,51,62] CL has

417   a distinctive conical shape with four fatty acyl chains, which allows it to create a highly curved

418   membrane environment in the IMM, promoting close packing of protein complexes that likely

419   facilitates supercomplex formation.[50] CL also directly interacts with various subunits of the ETC

420   complexes through electrostatic interactions, which help stabilize the supercomplexes by

421   anchoring them together in a specific spatial orientation to optimize electron flow.[48] Liver-

422   specific deletion of CLS only resulted in a lower abundance of the $I+III_2+IV_1$ supercomplex. We

423   interpret these findings to mean that $I+III_2+IV_1$ supercomplex is particularly sensitive to the

424   reduced CL level in hepatocytes.

425

426   In our study, we observed a striking correlation between CL levels and CoQ in human liver

427   samples from healthy/MASH patients (R_2 of 0.64). In contrast, low mitochondrial CL induced by

428   CLS deletion coincided with a greater mitochondrial CoQ content in CLS-LKO mice compared to

429   controls. These data likely suggest that acute and robust reduction in CLS or CL level might

430   trigger a compensatory CoQ production in mice. Conversely, because the samples from

431   healthy/MASH patients were from those who had cirrhosis, MASH samples likely came from

432   subjects that had suffered from years of MASLD pathology. In those samples, where reduction

433   in CL was quantitatively modest compared to what was induced with CLS knockout, CoQ might

434   have gradually decreased coincidental to the decrease in CL. Regardless of these differences in

435   mice and humans, it is clear that there is a relationship between CL and CoQ that is worth

436   further exploration.

437

438   In conclusion, our findings identify a critical role for CL in regulating ETC efficiency to promote

439   oxidative stress. In both mice and humans, MASLD is associated with a decrease in hepatic

440   mitochondrial CL, suggesting that low CL may be the cause of the obligatory increase in

441   oxidative stress known to occur with MASLD progression. We further link CL deficiency to

442   increased electron leak at the CoQ-complex III interface, and as the primary defect that

443   promotes oxidative stress. We believe that these bioenergetic changes underlie the

444   pathogenesis of MASLD, as CL deletion was sufficient to cause steatosis, fibrosis, and

445   inflammation, phenocopying many changes that occur with MASLD/MASH progression. Further

446   research will be needed to fully uncover how CL regulates CoQ, and to test whether rescuing

447   the CL/CoQ axis might be effective in treating patients with MASLD/MASH.

448 **Methods**

449 Experimental model and subject details

450 **Human participants**

451 De-identified liver samples were acquired from the University of Utah Biorepository and

452 Molecular Pathology Shared Resource from patients undergoing liver transplantation or

453 resection due to end-stage liver disease and/or liver tumor(s). All patients were classified to their

454 respective diagnosis by a pathologist at the time of initial collection. The diagnosis for individual

455 tissue samples was confirmed by a pathologist based on histology review of formalin-fixed,

456 paraffin-embedded sections takes from the same location as the tissue analyzed by targeted

457 lipid mass spectrometry.

458

459 **Mice**

460 All mice (male and female) used in this study were bred onto C57BL/6J background. CLS-LKO

461 mice were generated by crossing the CLS conditional knockout (CLScKO^{+/+}) generously

462 donated by Dr. Zachary Gerhart-Hines (University of Copenhagen)[24] with mice heterozygous for

463 Albumin promotor Cre (Alb-Cre^{+/-}) to produce liver-specific deletion of the CLS gene

464 (CLScKO^{+/+}, Alb-Cre^{+/-}) or control (CLScKO^{+/+}, no Cre) mice. CLScKO^{+/+} mice harbor loxP sites

465 that flank exon 4 of the CLS gene. For high-fat diet studies, 8 wk CLS-LKO and their respective

466 controls began high-fat diet (HFD, 42% fat, Envigo TD.88137) feeding for 8 wks. Mice were

467 fasted 4 hours and given an intraperitoneal injection of 80 mg/kg ketamine and 10 mg/kg

468 xylazine prior to terminal experiments and tissue collection. All animal experiments were

469 performed with the approval of the Institutional Animal Care and Use Committees at the

470 University of Utah.

471

472 **Cell lines**

473 Hepa 1-6 murine hepatoma cells were grown in high-glucose DMEM (4.5 g/L glucose, with L-

474 glutamine; Gibco 11965-092) supplemented with 10% FBS (heat-inactivated, certified, US

475 origin; Gibco 10082-147), and 0.1% penicillin-streptomycin (10,000 U/mL; Gibco 15140122). For

476 lentivirus-mediated knockdown of CLS, CLS expression was decreased using the pLKO.1

477 lentiviral-RNAi system. Plasmids encoding shRNA for mouse *Crls1* (shCLS: TRCN0000123937)

478 was obtained from MilliporeSigma. Packaging vector psPAX2 (ID 12260), envelope vector

479 pMD2.G (ID 12259), and scrambled shRNA plasmid (SC: ID 1864) were obtained from

480 Addgene. HEK293T cells in 10 cm dishes were transfected using 50 μL 0.1% polyethylenimine,

481 200 μL, 0.15 M sodium chloride, and 500 μL Opti-MEM (with HEPES, 2.4 g/L sodium

482 bicarbonate, and l-glutamine; Gibco 31985) with 2.66 μg of psPAX2, 0.75 μg of pMD2.G, and 3

483 μg of either scrambled or *Crls1* shRNA plasmid. Cells were selected with puromycin throughout

484 differentiation to ensure that only cells infected with shRNA vectors were viable.

485

486 Method details

487 **Body composition**

488 To assess body composition, mice were analyzed using a Bruker Minispec NMR (Bruker,

489 Germany) 1 week prior to terminal experiments. Body weights were measured and recorded

490 immediately prior to terminal experiments.

491

492 **RNA quantification**

493 For quantitative polymerase chain reaction (qPCR) experiments, mouse tissues were

494 homogenized in TRIzol reagent (Thermo Fisher Scientific) and RNA was isolated using

495 standard techniques. The iScript cDNA Synthesis Kit was used to reverse transcribe total RNA,

496 and qPCR was performed with SYBR Green reagents (Thermo Fisher Scientific). Pre-validated

497 primer sequences were obtained from mouse primer depot

498 (https://mouseprimerdepot.nci.nih.gov/). All mRNA levels were normalized to RPL32. For RNA

499   sequencing, liver RNA was isolated with the Direct-zol RNA Miniprep Plus kit (Zymo Cat#:

500   R2070). RNA library construction and sequencing were performed by the High-Throughput

501   Genomics Core at the Huntsman Cancer Institute, University of Utah. RNA libraries were

502   constructed using the NEBNext Ultra II Directional RNA Library Prep with rRNA Depletion Kit

503   (human, mouse rat). Sequencing was performed using the NovaSeq S4 Reagent Kit v1.5

504   150x150 bp Sequencing with >25 million reads per sample using adapter read 1:

505   AGATCGGAAGAGCACACGTCTGAACTCCAGTCA and adapter read 2:

506   AGATCGGAAGAGCGTCGTGTAGGGAAAGAGTGT. Pathway analyses were performed by the

507   Bioinformatics Core at the Huntsman Cancer Institute, University of Utah using the Reactome

508   Pathway Database. For differentially expressed genes, only transcripts with Padj < 0.05 and

509   baseMean > 100 are included.

510

511   **DNA isolation and quantitative PCR**

512   Genomic DNA for assessments of mitochondrial DNA (mtDNA) was isolated using a

513   commercially available kit according to the manufacturer's instructions (69504, Qiagen).

514   Genomic DNA was added to a mixture of SYBR Green (Thermo Fisher Scientific) and primers.

515   Sample mixtures were pipetted onto a 3840well plate and analyzed with QuantStudio 12K Flex

516   (Life Technologies). The following primers were used: mtDNA fwd, TTAAGA-CAC-CTT-GCC-

517   TAG-CCACAC; mtDNA rev, CGG-TGG-CTG-GCA-CGA-AAT-T; nucDNA fwd, ATGACG-ATA-

518   TCG-CTG-CGC-TG; nucDNA rev, TCA-CTT-ACC-TGGTGCCTA-GGG-C.

519

520   **Western blot analysis**

521   For whole liver lysate, frozen liver was homogenized in a glass homogenization tube using a

522   mechanical pestle grinder with homogenization buffer (50 mM Tris pH 7.6, 5 mM EDTA, 150

523   mM NaCl, 0.1% SDS, 0.1% sodium deoxycholate, 1% triton X-100, and protease inhibitor

524   cocktail). After homogenization, samples were centrifuged for 15 min at 12,000 × g. Protein

525 concentration of supernatant was then determined using a BCA protein Assay Kit (Thermo

526 Scientific). Equal protein was mixed with Laemmeli sample buffer and boiled for 5 mins at 95°C

527 for all antibodies except for OXPHOS cocktail antibody (at room temp for 5 mins), and loaded

528 onto 4–15% gradient gels (Bio-Rad). Transfer of proteins occurred on a nitrocellulose

529 membrane and then blocked for 1 hr. at room temperature with 5% bovine serum albumin in

530 Tris-buffered saline with 0.1% Tween 20 (TBST). The membranes were then incubated with

531 primary antibody (see Extended Data Table 2), washed in TBST, incubated in appropriate

532 secondary antibodies, and washed in TBST. Membranes were imaged utilizing Western

533 Lightning Plus-ECL (PerkinElmer) and a FluorChem E Imager (Protein Simple). For isolated

534 mitochondria, identical procedures were taken with equal protein of mitochondrial preps.

535

536 **Single cell preparation of liver tissue for flow cytometry**

537 After mice were euthanized using isoflurane, blood was collected by cardiac puncture, the

538 abdomen was exposed and the liver collected, rinse with PBS and weighed. Liver was

539 subsequently transferred in approximately 3ml of serum-free RPMI-1640 containing

540 Collagenase D (10mg/ml; Sigma) and DNase (1mg/ml; Sigma) and incubated in a rocking

541 platform for 45 min at 37°C. The liver extract was mashed through a 70μm filter, the cell re-

542 suspended in RPMI-1640 containing 10% FBS and centrifuged at 1600 rpm for 5 min. The

543 supernatant was discarded and the pellet re-suspended in approximately 4 ml of 70% Percoll,

544 then transferred in 15 ml conical tube, carefully overlayed with 4 ml of 30% Percoll and

545 centrifuged 1600 rpm for 25 min with the brake turned off. The non-parenchymal cells

546 suspension from the Percoll interface were removed and mixed with 10 mL of RPMI-1640

547 containing 10% FBS and the cells were centrifuged at 1600 rpm for 5 min. Red blood cells

548 (RBC) were removed from the pelleted single cell suspensions of livers non-parenchymal cells

549 by incubation in an ammonium chloride -based 1x RBC lysis buffer (Thermofisher, eBioscience).

550 The cells were again pelleted and mixed with FACS buffer (2% BSA, 2mM EDTA in PBS), then

551   stained with Zombie-NIR viability dye (BioLegend) per manufacturer's instructions to

552   discriminate live vs dead cells. To prevent non-specific Fc binding, the cells were incubated with

553   Fc Block (anti-mouse CD16/32, clone 93, Biolegend) for 15 min followed by the indicated

554   antibodies cocktail for 60 min in the dark on ice: CD45 (FITC, clone S18009F, Biolegend),

555   CD11b (BVC421, clone M1/70, Biolegend), F4/80 (APC, clone BM8, Biolegend), TIM4

556   (PerCP/Cy5.5, clone RMT4-54, Biolegend), Ly6C (PE, clone HK1.4, Biolegend), MHCII (BV605,

557   clone M5/114.15.2, Biolegend), CD11c (BV785, clone N418, Biolegend) and Ly6G (PE/Cy7,

558   clone 1A8, Biolegend). After surface staining, cells were fixed with a paraformaldehyde-based

559   fixation buffer (BioLegend). Flow cytometric acquisition was performed on a BD Fortessa X20

560   flow cytometer (BD Biosciences) and data analyzed using FlowJo software (Version 10.8.1;

561   Tree Star Inc).

562

563   **Glucose tolerance test**

564   Intraperitoneal glucose tolerance tests were performed by injection of 1 mg glucose per gram

565   body mass at least 6 days prior to sacrifice. Mice were fasted for 4 hours prior glucose injection.

566   Blood glucose was measured 30 minutes before glucose injection and at 0, 15, 30, 60, 90, and

567   120 minutes after injection via tail bleed with a handheld glucometer (Bayer Contour 7151H).

568

569   **Pyruvate tolerance test**

570   Pyruvate tolerance tests were performed by injection of 2 mg pyruvate per gram of body mass

571   in PBS adjusted to pH 7.3-7.5 at least 6 days prior to sacrifice. Blood glucose was measured 30

572   minutes before pyruvate injection and at 0, 15, 30, 45, 60, 75, 90, 105, and 120 minutes after

573   injection via tail bleed with a handheld glucometer (Bayer Contour 7151H).

574

575   **Electron microscopy**

576   To examine mitochondrial ultrastructure and microstructures, freshly dissected liver tissues from

577   CLS-LKO and their controls were sectioned into ≈2 mm pieces and processed by the Electron

578   Microscopy Core at University of Utah. To maintain the ultrastructure of the tissue via

579   irreversible cross-link formation, each section was submerged in fixative solution (1%

580   glutaraldehyde, 2.5% paraformaldehyde, 100 mM cacodylate buffer pH 7.4, 6 mM CaCl2, 4.8%

581   sucrose) and stored at 4°C for 48 hours. Samples then underwent 3 × 10-minute washes in 100

582   mM cacodylate buffer (pH 7.4) prior to secondary fixation (2% osmium tetroxide) for 1 hour at

583   room temperature. Osmium tetroxide as a secondary fixative has the advantage of preserving

584   membrane lipids, which are not preserved using aldehyde, alone. After secondary fixation,

585   samples were subsequently rinsed for 5 minutes in cacodylate buffer and distilled H_2O, followed

586   by prestaining with saturated uranyl acetate for 1 hour at room temperature. After prestaining,

587   each sample was dehydrated with a graded ethanol series (2 × 15 minutes each: 30%, 50%,

588   70%, 95%; then 3 × 20 minutes each: 100%) and acetone (3 × 15 minutes) and were infiltrated

589   with EPON epoxy resin (5 hours 30%, overnight 70%, 3 × 2-hour 40 minute 100%, 100% fresh

590   for embed). Samples were then polymerized for 48 hours at 60°C. Ultracut was performed using

591   Leica UC 6 ultratome with sections at 70 nm thickness and mounted on 200 mesh copper grids.

592   The grids with the sections were stained for 20 minutes with saturated uranyl acetate and

593   subsequently stained for 10 minutes with lead citrate. Sections were examined using a JEOL

594   1200EX transmission electron microscope with a Soft Imaging Systems MegaView III CCD

595   camera.

596

597   **Histochemistry**

598   A fresh liver tissue was taken from each mouse and immediately submerged in 4%

599   paraformaldehyde for 12 hours and then 70% ethanol for 48 hours. Tissues were sectioned at

600   10-µm thickness, embedded in paraffin, and stained for Masson's Trichrome to assess fibrosis

601   or hematoxylin and eosin (H&E) to determine fat droplet accumulation. Samples were imaged

602   on Axio Scan Z.1 (Zeiss).

603

604   **Native PAGE**

605   Isolated mitochondria (100 µg) suspended in MIM were pelleted at 12,000 x g for 15 min and

606   subsequently solubilized in 20 µL sample buffer (5 µL of 4x Native Page Sample Buffer, 8 µL

607   10% digitonin, 7 µL ddH$_2$O per sample) for 20 min on ice and then centrifuged at 20,000 x g for

608   30 mins at 4°C. 15 µL of the supernatant (75 µg) was collected and placed into a new tube and

609   mixed with 2 µL of G-250 sample buffer additive. Dark blue cathode buffer (50 mLs 20X Native

610   Page running buffer, 50 mLs 20x cathode additive, 900 mLs ddH$_2$O) was carefully added to the

611   front of gel box (Invitrogen Mini Gel Tank A25977) and anode buffer (50 mLs 20x Native Page

612   running buffer to 950 mL ddH$_2$O) was carefully added to the back of the gel box making sure to

613   not mix. The samples were then loaded onto a native PAGE 3-12% Bis-Tris Gel (BN1001BOX,

614   Thermo Fisher Scientific), and electrophoresis was performed at 150 V for 1 hour on ice. The

615   dark blue cathode buffer was carefully replaced with light blue cathode buffer (50 mLs 20X

616   Native Page running buffer, 5 mL 20X cathode additive to 945 mLs ddH$_2$O) and run at 30 V

617   overnight at 4°C. Gels were subsequently transferred to PVDF at 100 V, fixed with 8% acetic

618   acid for 5 min, washed with methanol, and blotted with the following primary antibodies Anti-

619   GRIM19 (mouse monoclonal; ab110240), Anti-SDHA (mouse monoclonal; ab14715), Anti-

620   UQCRFS1 (mouse monoclonal; ab14746), Anti-MTCO1 (mouse monoclonal; ab14705), Anti-

621   ATP5a (mouse monoclonal; ab14748), Anti-NDUFA9 (mouse monoclonal; ab14713) in 5% non-

622   fat milk in TBST. Secondary anti-mouse HRP antibody listed in the key resources table and

623   Western Lightning Plus-ECL (PerkinElmer NEL105001) was used to visualize bands.

624

625   **Isolation of mitochondrial and cytosolic fractions**

626   Liver tissues were minced in ice-cold mitochondrial isolation medium (MIM) buffer [300 mM

627   sucrose, 10 mM Hepes, 1 mM EGTA, and bovine serum albumin (BSA; 1 mg/ml) (pH 7.4)] and

628   gently homogenized with a Teflon pestle. To remove excess fat in the samples, an initial high-

629   speed spin was performed on all samples: homogenates were centrifuged at 12,000 x g for 10

630   mins at 4°C, fat emulsion layers were removed and discarded, and resulting pellets were

631   resuspended in MIM + BSA. Samples were then centrifuged at 800 x g for 10 min at 4°C. The

632   supernatants were then transferred to fresh tubes and centrifuged again at 1,300 x g for 10 min

633   at 4°C. To achieve the mitochondrial fraction (pellet), the supernatants were again transferred to

634   new tubes and centrifuged at 12,000 x g for 10 min at 4°C. The resulting crude mitochondrial

635   pellets were washed three times with 0.15 M KCl to remove catalase, and then spun a final time

636   in MIM. The final mitochondrial pellets were resuspended in MIM buffer for experimental use.

637   For cytosolic fraction, the supernatant from 12,000 x g spin was ultracentrifuged at 180,000 x g

638   for 16 hours in a fixed angle rotor (FIBERLite, F50L-24x1.5). The top half of the supernatant

639   was collected as analyzed as the cytosolic fraction for western blotting analyses.

640

Mitochondrial respiration measurements

642   Mitochondrial O_2 utilization was measured using Oroboros O2K Oxygraphs. Isolated

643   mitochondria (50 µg for TCA substrate respiration and 100 µg for fatty acid respiration) were

644   added to the oxygraph chambers containing assay buffer Z (MES potassium salt 105 mM, KCl

645   30 mM, KH_2PO_4 10 mM, $MgCl_2$ 5 mM, BSA 1 mg/ml). Respiration was measured in response to

646   the following substrates: 0.5 mM malate, 5 mM pyruvate, 2.5 mM ADP, 10 mM succinate, 1.5

647   µM FCCP, 0.02 mM palmitoyl-carnitine, 0.5 mM malate.

648

Mitochondrial JH$_2$O$_2$

650   Mitochondrial H_2O_2 production was determined in isolated mitochondria from liver tissue using

651   the Horiba Fluoromax-4/The Amplex UltraRed (10 µM)/horseradish peroxidase (3 U/ml)

652 detection system (excitation/emission, 565:600, HORIBA Jobin Yvon Fluorolog) at 37°C.

653 Mitochondrial protein was placed into a glass cuvette with buffer Z supplemented with 10 mM

654 Amplex UltraRed (Invitrogen), 20 U/mL CuZn SOD). Since liver tissue is capable of producing

655 resorufin from amplex red (AR), without the involvement of horseradish peroxidase (HRP) or

656 H_2O_2, phenylmethylsulfonyl fluoride (PMSF) was included to the experimental medium due to its

657 ability to inhibit HRP-independent conversion of AR to resorufin.[63] PMSF was added to the

658 cuvette immediately prior to measurements and at a concentration that does not interfere with

659 biological measurements (100 µM).[63] A 5-min background rate was obtained before adding 10

660 mM succinate to the cuvette to induce H_2O_2 production. After 4 min, 100 µM 1,3-bis(2-

661 chloroethyl)-1-nitrosourea (BCNU) was added to the cuvette with 1 µM auranofin to inhibit

662 glutathione reductase and thioredoxin reductase, respectively. After an additional 4 min, the

663 assay was stopped, and the appearance of the fluorescent product was measured.

664

665 Site-specific electron leak was measured by systematically stimulating each site while inhibiting

666 the other three.[54] Site I_F was investigated in the presence of 4 mM malate, 2.5 mM ATP, 5 mM

667 aspartate, and 4 µM rotenone; site I_Q was measured as a 4 µM rotenone-sensitive rate in the

668 presence of 5 mM succinate; site III_{QO} was measured as a 2 µM myxothiazol-sensitive rate in

669 the presence of 5 mM succinate, 5 mM malonate, 4 µM rotenone, and 2 µM antimycin A; and

670 site II_F was measured as the 1 mM malonate-sensitive rate in the presence of 0.2 mM succinate

671 and 2 µM myxothiazol. As previously mentioned, electron leak is quantified using Amplex Red in

672 the presence of excess superoxide dismutase, such that both superoxide and hydrogen

673 peroxide production are accounted for by a change in fluorescence intensity (JH_2O_2) using high-

674 resolution fluorometry (Horiba Fluoromax4®).

675

676 **Lipid mass spectrometry for reduced and oxidized CoQ**

677   Liver tissue was homogenized in ice cold isolation buffer (250 mM sucrose, 5 mM Tris-HCl, 1

678   mM EGTA, 0.1% fatty acid free BSA, pH 7.4, 4°C) using a tissuelyser. Mitochondria were then

679   isolated via differential centrifugation (800 x g for 10 min, 1300 x g for 10 min, 12,000 x g for 10

680   min at 4°C), flushing each step under a stream nitrogen to prevent oxidation. Protein content

681   was determined by bicinchoninic acid assay using the Pierce BCA protein assay with bovine

682   serum albumin as a standard. To extract CoQ from mitochondria, incubations of 100 µg

683   mitochondrial protein in 250 µL ice-cold acidified methanol, 250 µL hexane, and 1146 pmol per

684   sample of CoQ standard (Cambridge Isotope Laboratories, CIL DLM-10279) were vortexed. The

685   CoQ-containing hexane layer was separated by centrifugation (10 min, 17,000 x g, 4°C) and

686   then dried down under a stream of nitrogen. Dried samples were then resuspended in methanol

687   containing 2 mM ammonium formate and transferred to 1.5 mL glass mass spectrometry vials.

688   Liquid chromatography-mass spectrometry (LC-MS/MS) was then performed on the

689   reconstituted lipids using an Agilent 6530 UPLC-QTOF mass spectrometer.

690

691   U-^{13}C-glucose and U-^{13}C-palmitate labeling in hepa1-6 cell line

692   Stable isotope tracing experiments were conducted using U-^{13}C-glucose or U-^{13}C-palmitate to

693   assess metabolic fluxes in hepa1-6 cells with or without CLS knockdown. Cells were incubated

694   in either U-^{13}C-glucose or U-^{13}C-palmitate for 4 hours. For palmitate incubations, U-^{13}C-

695   palmitate was conjugated to fatty acid-free bovine serum albumin (BSA) and supplemented with

696   1 mM carnitine prior to being added to the culture medium. Following the 4-hour incubation

697   period, cells were washed once with 1 mL of ice-cold Dulbecco's Phosphate Buffered Saline

698   (dPBS) and then scraped in 0.7 mL ice-cold dPBS. The cells were pelleted by centrifugation at

699   500 x g for 5 minutes at 4°C, and the supernatant was carefully removed. Cell pellets were

700   resuspended in 215 µL of ice-cold dPBS and sonicated on ice using a 1/8" probe sonicator at

701   30% amplitude for 6 seconds. Debris was lightly pelleted by centrifugation at 500 x g for 2

702   minutes at 4°C. From the resulting supernatant, 25 µL was transferred to a separate tube for

703   protein quantification using the bicinchoninic acid (BCA) assay. Samples incubated with U-^{13}C-

704   glucose were submitted for gas chromatography-mass spectrometry (GC-MS) and liquid

705   chromatography-mass spectrometry (LC-MS) analysis, while those incubated with U-^{13}C-

706   palmitate were submitted for GC-MS analysis only.

707

708   **GC-MS**

709   All GC-MS analysis was performed with an Agilent 5977b GC-MS MSD-HES and an Agilent

710   7693A automatic liquid sampler. Dried samples were suspended in 40 µL of a 40 mg/mL O-

711   methoxylamine hydrochloride (MOX) (MP Bio #155405) in dry pyridine (EMD Millipore

712   #PX2012-7) and incubated for one hour at 37 °C in a sand bath. 25 µL of this solution was

713   added to auto sampler vials. 60 µL of N-methyl-N-trimethylsilyltrifluoracetamide (MSTFA with

714   1% TMCS, Thermo #TS48913) was added automatically via the auto sampler and incubated for

715   30 minutes at 37 °C. After incubation, samples were vortexed and 1 µL of the prepared sample

716   was injected into the gas chromatograph inlet in the split mode with the inlet temperature held at

717   250 °C. A 10:1 split ratio was used for analysis for most metabolites. Any metabolites that

718   saturated the instrument at the 10:1 split was analyzed at a 100:1 split ratio. The gas

719   chromatograph had an initial temperature of 60 °C for one minute followed by a 10 °C/min ramp

720   to 325 °C and a hold time of 10 minutes. A 30-meter Agilent Zorbax DB-5MS with 10 m

721   Duraguard capillary column was employed for chromatographic separation. Helium was used as

722   the carrier gas at a rate of 1 mL/min.

723

724   Data were collected using MassHunter software (Agilent). Metabolites were identified and their

725   peak area was recorded using MassHunter Quant. This data was transferred to an Excel spread

726   sheet (Microsoft, Redmond WA). Metabolite identity was established using a combination of an

727   in-house metabolite library developed using pure purchased standards, the NIST library and the

728 Fiehn library. There are a few reasons a specific metabolite may not be observable through GC-

729 MS.

730

731 **LC-MS**

732 A pooled quality control (QC) sample for each sample type was prepared by combining 10 µL of

733 each sample. Samples were randomized prior to analysis. A SCIEX 7600 Zeno-ToF (AB SCIEX

734 LLC, Framingham, MA, USA) coupled to an Agilent 1290 Infinity II HPLC system in positive-

735 ionization modes was used for analysis. Separation was achieved using a Waters BEH zhilic 2.1

736 x 100 mm column (Waters Corporation, Milford, MA, USA) with Phenomenex Krudkatcher Ultra

737 (Phenomenex, Torrence, CA, USA). Buffers consisted of 99% ACN with 5% ddH2O (buffer B)

738 and 5% 25 mM ammonium carbonate in ddH2O (buffer A). An initial concentration of 99% buffer

739 B was decreased to 85% over 2 min, then further decreased to 75%, and 60% over 3-minute

740 intervals. Next, buffer B was decreased to 40% and held for 1 min. Then Buffer B was

741 decreased to 1% and held for 1 min. Eluents were returned to initial conditions over 0.1 min,

742 and the system was allowed to equilibrate for 5 min between runs. Mass spectrometry analysis

743 was performed by high-resolution multiple reaction monitoring (MRM HR).

744

745 Data was collected using SCIEX analyst. Chromatogram integration was performed using

746 SCIEX MultiQuant. This data was transferred to an Excel spread sheet (Microsoft, Redmond

747 WA). Statistical analysis was performed using Microsoft Excel Data Analysis add-in. The

748 metabolite lists were curated to the metabolites of interest for the researcher as applicable.

749 Metabolite identity was established using a combination of an in-house metabolite library

750 developed using pure purchased standards and the human metabolite data base (hmdb.ca).

751 Isotope correction was performed using in-house software.

752

753 **Mitochondrial phospholipids enrichment**

754   Isolated mitochondria (500 µg) from 2-month-old mice were incubated in fusion buffer [220 mM

755   mannitol, 70 mM sucrose, 2 mM Hepes, 10 mM KH2PO4, 5 mM MgCl2, 1 mM EGTA, 10 mM

756   glutamate, 2 mM malate, 10 mM pyruvate, and 2.5 mM ADP (pH 6.5)] for 20 min at 30°C under

757   constant stirring agitation in the presence of 15 nmol of small unilamellar vesicles (SUVs) (CL

758   from Avanti Polar Lipids, 840012; PC from Avanti Polar Lipids, 850375C). After fusion,

759   mitochondria were layered on a sucrose gradient (0.6 M) and centrifuged 10 min at 10,000g at

760   4°C to remove SUV. Pellet was then washed in mitochondrial buffer [250 mM sucrose, 3 mM

761   EGTA, and 10 mM tris-HCl, (pH 7.4)].

762

Serum AST and ALT

763

764   Mice were sacrificed by CO_2 inhalation and blood samples collected via cardiac puncture into

765   heparin-coated tubes and centrifuged for collection of plasma within 1 hour of blood collection

766   and frozen at -80°C until analysis. Plasma samples from mice were processed in a single batch

767   for determination of serum alanine aminotransferase (ALT) and aspartate aminotransferase

768   (AST) levels using a DC Element chemistry analyser (HESKA).

769

Quantification and statistical analyses

770

771   The level of significance was set at $p < 0.05$. Student's T tests were used to determine the

772   significance between experimental groups and two-way ANOVA analysis followed by a within-

773   row pairwise comparison post hoc test where appropriate. For Student's T tests, Gaussian

774   distribution was assumed as well as assuming both populations had the same standard

775   deviation. The sample size (n) for each experiment is shown in the figure legends and

776   corresponds to the sample derived from the individual mice or for cell culture experiments on an

777   individual batch of cells. Unless otherwise stated, statistical analyses were performed using

778   GraphPad Prism software.

779

780 **Materials availability**

781 Plasmids utilized by this study are available from Sigma Aldrich. Mouse lines generated by this

782 study may be available at personal request from the lead contact. No new reagents were

783 created or used by this study.

784

785 **Data and code availability**

786 All data are available in the main text or the Extended Data. Code for RNA sequencing can be

787 retrieved upon request.

Figure Legends

Fig. 1. Hepatic mitochondrial phospholipidome in mouse models of MASLD

(a) A schematic for performing mitochondrial phospholipidomic analyses in liver samples from humans. (b) Representative H&E staining from individuals with healthy or MASH liver. (c) Hepatic mitochondrial CL levels from healthy controls or individuals with MASH (n=10 and 16 per group). (d) Hepatic mitochondrial PG levels from healthy controls or individuals with MASH (n=10 and 16 per group). (e) Pathway for CL biosynthesis. (f) Representative H&E staining of livers from mice given standard chow or a Western HFD for 16 wks.(g) Representative H&E staining of livers from 20 wk old wildtype or ob/ob mice. (h) Representative Masson's Trichrome staining of livers from mice given standard chow or GAN diet for 30wks. (i) Representative Masson's Trichrome staining of livers from mice injected with vehicle or carbon tetrachloride for 6wks.(j) Representative western blot of OXPHOS subunits and citrate synthase in liver tissues from mice given standard chow or a Western HFD for 16 wks. (k) Representative western blot of OXPHOS subunits and citrate synthase in liver tissues from 20 wk old wildtype or ob/ob mice . (l) Representative western blot of OXPHOS subunits and citrate synthase in liver tissues from mice given standard chow or the GAN diet for 30 wks. (m) Representative western blot of OXPHOS subunits and citrate synthase in liver tissues from mice injected with vehicle or carbon tetrachloride for 6 wks.(n) A heatmap of hepatic mitochondrial phospholipidome of mice given standard chow or HFD for 16 wks. (o) A heatmap of hepatic mitochondrial phospholipidome of 20 wk old wildtype or ob/ob mice. (p) A heatmap of hepatic mitochondrial phospholipidome of mice given standard chow or the GAN diet for 30 wks. (q) A heatmap of hepatic mitochondrial phospholipidome of mice injected with vehicle or carbon tetrachloride for 6 wks. (r) Venn Diagram comparing hepatic mitochondrial phospholipidome from all four models of MASLD: HFD, ob/ob, GAN, or carbon tetrachloride. (s) CLS mRNA levels in livers of mice given standard chow or a Western HFD for 16 wks (n=4 per group). (t) CLS mRNA levels in livers from 20 wk old wildtype or ob/ob mice (n=6 per group). (u) CLS mRNA levels in livers from mice given

814   standard chow or the GAN diet for 30 wks (*n*=5 per group).(v) CLS mRNA levels in livers from

815   mice injected with vehicle or carbon tetrachloride for 6 wks (*n*=6 and 5 per group). Statistical

816   significance was determined by 2-way ANOVA with a within-row pairwise comparison (c, d, n, o,

817   p, and q) and unpaired, two-sided Student's T test (c and d insert, s, t, u, and v). Measurements

818   were taken from distinct samples for all groups.

819

820   **Fig. 2. Hepatocyte-specific deletion of CLS induces MASLD/MASH**

821   (a) A schematic for hepatocyte-specific deletion of CLS in mice. (b) CLS mRNA levels in livers

822   from control and CLS-LKO mice (*n*=5 and 7 per group). (c) Mitochondrial CL levels in liver from

823   control and CLS-LKO mice (*n*=5 and 6 per group). (d) Body mass of control and CLS-LKO mice

824   (*n*=13 and 11 per group). (e) Body composition of control and CLS-LKO mice (*n*=6 and 7 per

825   group). (f) Liver mass of control and CLS-LKO mice (*n*=10 and 13 per group). (g)

826   Representative H&E staining of livers from control and CLS-LKO mice. (h) Representative

827   Masson's Trichrome staining of livers from control and CLS-LKO mice. (i) An RNAseq-derived

828   heatmap of select genes associated with MASH, liver regeneration, and HCC for control and

829   CLS-LKO mice (*n*=7 and 5 per group). (j) Serum AST for control and CLS-LKO mice (*n*=6 and 7

830   per group). (k) Serum ALT for control and CLS-LKO mice (*n*=6 and 7 per group). (l) mRNA

831   levels of TNFα, TGFβ, IL-12, and MCP1 in livers from control and CLS-LKO mice (*n*=5 and 7

832   per group). (m) Representative image of flow cell population gating for livers from control and

833   CLS-LKO mice (*n*=5 and 7 per group). (n) cDC2 cell population in livers from control and CLS-

834   LKO mice (*n*=5 and 7 per group). (o) F4/80+ cell population in livers from control and CLS-LKO

835   mice (*n*=5 and 7 per group). (p) Ly6C^{hi} inflammatory monocyte population in livers from control

836   and CLS-LKO mice (*n*=5 and 7 per group). (q) MHC-II cell population in control and CLS-LKO

837   livers (*n*=5 and 7 per group). (r) Neutrophil cell population in control and CLS-LKO livers (*n*=5

838   and 7 per group). (s) cDC1 cell population in control and CLS-LKO livers (*n*=5 and 7 per group).

839   All results are from mice fed with standard chow. Statistical significance was determined by 2-

840   way ANOVA with a within-row pairwise comparison (c and l) and unpaired, two-sided Student's

841   T test (b, d, e, f, i-adjusting for FDR, and j-s). Data represent mean + SEM (b, c, d-f, j-l, and n-s).

842   Measurements taken for b and c were from the same samples. Measurements for d, e, f, g, h,

843   and i were taken from distinct samples. Measurements taken for j, k, m-s were from the same

844   samples. Measurements taken for l were from distinct samples.

845

846   **Fig. 3. CLS deletion increases mitochondrial respiratory capacity**

847   (a) Glucose tolerance test (IPGTT) of control and CLS-LKO mice fed with standard chow (n=6

848   and 7 per group). (b) Area under the curve for IPGTT. (c) Pyruvate tolerance test (PTT) of

849   control and CLS-LKO mice fed with standard chow (n=6 and 8 per group). (d) Area under the

850   curve for PTT. (e) An RNAseq-derived heatmap of genes associated with lipogenesis, VLDL,

851   and β-oxidation for control and CLS-LKO mice (n=6 and 5 per group). (f) An RNAseq-derived

852   heatmap of genes associated with components of ETS complex structure and function (n=6 and

853   5 per group). (g) Representative electron microscopy images of liver mitochondria from control

854   and CLS-LKO mice. (h) Representative western blot of whole liver tissue lysate using OXPHOS

855   cocktail and citrate synthase in control and CLS-LKO mice. (i) Ratio of mitochondrial to nuclear

856   DNA in liver tissue of control and CLS-LKO mice (n=8 per group). (j) Representative tracing

857   from high-resolution respirometry during maximal respiration using TCA cycle intermediates. (k)

858   JO$_2$ consumption in isolated liver mitochondria from control and CLS-LKO mice in response to

859   0.5 mM malate, 5 mM pyruvate, 2.5 mM ADP, 10 mM succinate, and 1.5 µM FCCP (n=6 per

860   group). (l) JO$_2$ consumption in isolated liver mitochondria from control and CLS-LKO mice in

861   response to 0.02 mM palmitoyl-carnitine, 0.5 mM malate, and 2.5 mM ADP (n=6 per group). (m)

862   Representative western blot of isolated mitochondria using OXPHOS cocktail in control and

863   CLS-LKO mice. All results are from mice fed with standard chow. Statistical significance was

864   determined by 2-way ANOVA with a within-row pairwise comparison (a, c, k, and l) and

865   unpaired, two-sided Student's T test (b, d, e and f- adjusting for FDRs, and i). Data represent

866   mean + SEM (a-d, k, and l). Data in box-and-whiskers plot in i represent median with min-to-

867   max. Measurements for a, c, g, and i were taken from distinct samples. Measurements from e

868   and f were from the same samples. Measurements from k, l, and m were taken using the same

869   samples.

870

871   **Fig. 4. Stable isotope tracing with [U-^{13}C] palmitate and [U-^{13}C] glucose in hepa1-6 cells**

872   **with or without CLS deletion**

873   (a) Schematic illustration of the labeling process during stable isotope tracing with [U-^{13}C]

874   palmitate or [U-^{13}C] glucose. Blue or green circles represent ^{13}C-labeled carbons, and red

875   circles represent unlabeled ^{12}C carbons. The pathway shows the flow from palmitate to beta-

876   oxidation or glucose through glycolysis to the tricarboxylic acid (TCA) cycle, with key

877   intermediates labeled. (b) Levels of labeled succinate from palmitate tracing in hepa1-6 cells

878   without (shSC) or with CLS deletion (shCLS) (n=6 per group). (c) Levels of labeled malate from

879   palmitate tracing in hepa1-6 cells without (shSC) or with CLS deletion (shCLS) (n=6 per group).

880   (d) Levels of labeled fumarate from palmitate tracing in hepa1-6 cells without (shSC) or with

881   CLS deletion (shCLS) (n=6 per group). (e) Levels of labeled pyruvate from glucose tracing in

882   hepa1-6 cells without (shSC) or with CLS deletion (shCLS) (n=6 per group). (f) Levels of labeled

883   acetyl-CoA from glucose tracing in hepa1-6 cells without (shSC) or with CLS deletion (shCLS)

884   (n=6 per group). (g) Levels of labeled lactate from glucose tracing in hepa1-6 cells without

885   (shSC) or with CLS deletion (shCLS) (n=6 per group). (h) Levels of labeled succinate from

886   glucose tracing in hepa1-6 cells without (shSC) or with CLS deletion (shCLS) (n=6 per group).

887   (i) Levels of labeled fumarate from glucose tracing in hepa1-6 cells without (shSC) or with CLS

888   deletion (shCLS) (n=6 per group). (j) Levels of labeled citrate from glucose tracing in hepa1-6

889   cells without (shSC) or with CLS deletion (shCLS) (n=6 per group). Statistical significance was

890   determined by unpaired, two-sided Student's T test. Data represent mean $\pm$ SEM.

891   Measurements were taken from the same samples for b-d and a different set of samples for e-j.

892

Fig. 5. CL deficiency promotes mitochondrial electron leak

(a) Representative electron microscopy images for control and CLS-LKO mice depicting fibrosis with red arrows. (b) mRNA levels of fibrotic markers (Col1a1 and Desmin) in liver tissues from control and CLS-LKO mice (n=5 and 7 per group). (c) Levels of cleaved caspase-3 in liver tissues from control and CLS-LKO mice (n=4 per group). (d) Levels of cleaved caspase-7 in liver tissues from control and CLS-LKO mice (n=4 per group). (e) Levels of mitochondrial cytochrome c in liver tissues of control and CLS-LKO mice (n=7 per group). (f) Levels of cytosolic cytochrome c levels in liver tissues of control and CLS-LKO mice (n=7 per group). (g) H_2O_2 emission and production in isolated liver mitochondria from control and CLS-LKO mice stimulated with succinate, or succinate, auranofin, and BCNU (n=3 and 4 per group). (h) Schematic representation of small unilamellar vesicles (SUVs) containing either cardiolipin (CL) or phosphatidylcholine (PC) to enrich mitochondria with exogenous lipids. (i) H_2O_2 production in liver mitochondria enriched with CL or PC SUVs in control and CLS-LKO mice (n=4 per group). All results are from mice fed with standard chow. Statistical significance was determined by 2-way ANOVA with a within-row pairwise comparison (b, g, and i) and unpaired, two-sided Student's T test (c-f). Data represent mean $\pm$ SEM. Measurements from a, b, g, and i are from distinct samples. Measurements from c and d were taken from the same samples. Measurements from e and f were taken from a different set of samples.

911

Fig. 6. Influence of CL deficiency on respiratory supercomplexes

(a) Representative western blot of respiratory supercomplexes detected using supercomplex antibody cocktail in isolated mitochondria from livers taken from control and CLS-LKO mice. (b) Representative western blot of respiratory supercomplex detected using GRIM19/complex I antibody in isolated mitochondria from livers taken from control and CLS-LKO mice (n=4 per group). (c) Quantification of b. (d) Representative western blot of respiratory supercomplex

918   detected using the NDUFA9/complex I antibody in isolated mitochondria from livers taken from

919   control and CLS-LKO livers (n=4 per group). (e) Quantification of d. (f) Representative western

920   blot of respiratory supercomplex detected using the SDHA2/complex II antibody in isolated

921   mitochondria from livers taken from control and CLS LKO livers (n=4 per group). Complex II is

922   not thought to form respiratory supercomplexes. (g) Quantification of f. (h) Representative

923   western blot of respiratory supercomplex detected using the UQCRFS1/complex III antibody in

924   isolated mitochondria from livers taken from control and CLS-LKO livers (n=4 per group). (i)

925   Quantification of h. (j) Representative western blot of respiratory supercomplex detected using

926   the MTCO1/complex IV antibody in isolated mitochondria from livers taken from control and

927   CLS-LKO livers (n=4 per group). (k) Quantification of j. (l) Representative western blot of

928   respiratory supercomplex detected using the ATP5A/complex V antibody in isolated

929   mitochondria from livers taken from control and CLS-LKO livers (n=4 per group). (m)

930   Quantification of l. All results are from mice fed with standard chow. Statistical significance was

931   determined by 2-way ANOVA with a within-row pairwise comparison (first panel in c, first panel

932   in e, first panel in i, and first panel in k) and unpaired, two-sided Student's T test (second panel

933   in c, second panel in e, g, second panel in i, second panel in k, and both panels in m). Data

934   represent mean $\pm$ SEM. Measurements from a-m were taken from the same samples.

935

936   **Fig. 7. CL deficiency disrupts coenzyme Q homeostasis in mice and humans**

937   (a) A schematic for site-specific electron leak. (b) Electron leak at site I_Q in liver mitochondria

938   from control and CLS-LKO mice (n=7 per group). (c) Electron leak at site I_F in liver mitochondria

939   from control and CLS-LKO mice (n=7 per group. (d) Electron leak at site II_F in liver mitochondria

940   from control or CLS-LKO mice (n=7 per group). (e) Electron leak at site III_{Q0} in liver mitochondria

941   from control or CLS-LKO mice (n=7 per group). (f) Oxidized coenzyme Q (CoQ) (ubiquinone)

942   can be charged with electrons to become reduced CoQ (ubiquinol). (g) Oxidized CoQ levels in

943   isolated mitochondrial fractions from livers taken from control and CLS-LKO mice (n=7 per

944   group). (h) Reduced CoQ levels in isolated mitochondrial fractions from livers taken from control

945   and CLS-LKO livers (*n*=7 per group). (i) CoQ levels in in isolated mitochondria from livers of

946   healthy human controls or patients with advanced steatohepatitis (*n*=10 and 16 per group). (j)

947   Pearson correlation analysis of CL and CoQ levels in human liver samples (R^2 = 0.64). Data

948   from b-e,g,h are from mice fed with standard chow. Statistical significance was determined by

949   unpaired two-sided Student's T test (b-e and insert in i) and 2-way ANOVA with a within-row

950   pairwise comparison (g, h, i). Data represent mean $\pm$ SEM (b-e, g, h, i). Measurements from b-e

951   were taken from the same samples. Measurements from g and h were taken from the same

952   samples. Measurements from i and j are from the same samples.

References

1. Younossi, Z.M., *et al.* Global epidemiology of nonalcoholic fatty liver disease—Meta-analytic assessment of prevalence, incidence, and outcomes. *Hepatology* **64**, 73-84 (2015).

2. Miao, L.T., Giovanni; Byrne, Christopher D; Cao, Ying-Ying; Zheng, Ming-Hua. Current status and future trends of the global burden of MASLD. *Trends in Endocrinology & Metabolism* **29**, 1043-2760 (2024).

3. Saito, K., *et al.* Characterization of hepatic lipid profiles in a mouse model with nonalcoholic seatohepatitis and subsequent fibrosis. *Scientific Reports* **5**(2015).

4. John, B.S.S. Nonalcoholic Steatohepatitis (NASH). in *StatPearls* (StatPearls Publishing, Treasure Island, 2023).

5. Vigano, L., Lleo, A. & Aghemo, A. Non-alcoholic fatty liver disease, non-alcoholic steatohepatitis, metabolic syndrome and hepatocellular carcinoma—a composite scenario. *Hepatobiliary Surgery and Nutrition* **7**, 130-133 (2018).

6. Fan, J.-G. & Cao, H.-X. Role of diet and nutritional management in non-alcoholic fatty liver disease. *Gastroenterology and Hepatology* **28**, 87-87 (2013).

7. Gordon, D.L., *et al.* Biomarkers of NAFLD progression: a lipidomics approach to an epidemic. *Journal of Lipid Research* **56**, 722-736 (2015).

8. Fu, S., *et al.* Aberrant lipid metabolism disrupts calcium homeostasis causing liver endoplasmic reticulum stress in obesity. *Nature* **473**, 528-531 (2011).

9. Simoes, I.C.M., Fontes, A., Pinton, P., Zischka, H. & Wieckowski, M.R. Mitochondria in non-alcoholic fatty liver disease. *The International Journal of Biochemistry & Cell Biology* **95**, 93-99 (2018).

10. Leveille, M. & Estall, J.L. Mitochondrial Dysfunction in the Transition from NASH to HCC. *Metabolites* **9**, 233 (2019).

11. Einer, C., *et al.* Mitochondrial adaptation in steatotic mice. *Mitochondrion* **59**, 483-495 (2018).

12. Sunny, N.E., Bril, F. & Cusi, K. Mitochondrial Adaptation in Nonalcoholic Fatty Liver Disease: Novel Mechanisms and Treatment Strategies. *Trends in Endocrinology & Metabolism* **28**(2018).

13. Noureddin, M. & Sanyal, A.J. Pathogenesis of NASH: the Impact of Multiple Pathways. *Current Hepatology Reports* **17**, 350-360 (2018).

14. Pfeiffer, K., *et al.* Cardiolipin stabilizes respiratory chain supercomplexes. *Metabolism and Bioenergetics* **278**, 52873-52880 (2003).

15. Johnson, J.M., *et al.* Targeted overexpression of catalase to mitochondria does not prevent cardioskeletal myopathy in Barth syndrome. *Journal of Molecular and Cellular Cardiology* **121**, 94-102 (2018).

16. Houtkooper, R.H. & Vaz, F.M. Cardiolipin, the heart of mitochondrial metabolism. *Cell. Mol. Life Sci.* **65**, 2493-2506 (2008).

17. Schlame ab, M. & Hostetler, K.Y. Cardiolipin synthase from mammalian mitochondria. *Biochimica et Biophysica Acta (BBA) - Molecular and Cell Biology of Lipids* **1348**, 207-213 (1997).

18. Paradies, G., Paradies, V., Ruggiero, F.M. & Petrosillo, G. Role of Cardiolipin in Mitochondrial Function and Dynamics in Health and Disease: Molecular and Pharmacological Aspects. *Cells* **8**, 728 (2019).

19. Funai, K., Summers, S.A. & Rutter, J. Reign in the membrane: How common lipids govern mitochondrial function. *Current Opinion in Cell Biology* **63**, 162-173 (2020).

20. Jussupow, A., Luca, A.D. & Kaila, V.R. How cardiolipin modulates the dynamics of respiratory complex I. *Science Advances* **5**(2019).

21. Schwall, C.T., Greenwood, V.L. & Alder, N.N. The stability and activity of respiratory Complex II is cardiolipin-dependent. *Biochimica et Biophysica Acta (BBA) - Molecular and Cell Biology of Lipids* **1817**, 1588-1596 (2012).

22. Bazan, S*., et al.* Cardiolipin-dependent Reconstitution of Respiratory Supercomplexes from Purified Saccharomyces cerevisiae Complexes III and IV*. **288**, 401-411 (2013).

23. Dudek, J*., et al.* Cardiolipin deficiency affects respiratory chain function and organization in an induced pluripotent stem cell model of Barth syndrome. *Stem Cell Research* **11**, 806-819 (2013).

24. Sustarsic, E.G*., et al.* Cardiolipin Synthesis in Brown and Beige Fat Mitochondria Is Essential for Systemic Energy Homeostasis. *Cell Metab* **28**, 159-174 (2018).

25. Jiang, F*., et al.* Absence of cardiolipin in the crd1 null mutant results in decreased mitochondrial membrane potential and reduced mitochondrial function. *Journal of Biological Chemistry* **275**, 22387-22394 (2000).

26. Xu, Y., Sutachan, J.J., Plesken, H., Kelley, R.I. & Schlame, M. Characterization of lymphoblast mitochondria from patients with Barth syndrome. *Laboratory Investigation; a journal of technical methods and pathology* **85**, 823-830 (2005).

27. Hsu, P*., et al.* Cardiolipin remodeling by TAZ/tafazzin is selectively required for the initiation of mitophagy. *Autophagy* **11**, 643-652 (2015).

28. Le, C.H*., et al.* Tafazzin deficiency impairs CoA-dependent oxidative metabolism in cardiac mitochondria. *Journal of Biological Chemistry* **295**, 12485-12497 (2020).

29. Heden, T.D*., et al.* Mitochondrial PE potentiates respiratory enzymes to amplify skeletal muscle aerobic capacity. *Science Advances* **5**, 8352 (2019).

30. Johnson, J.M.P., Alek D; Balderas, Enrique; Sustarsic, Elahu G; Maschek, J Alan; Brothwell, Marisa J; Alejandro, Jara-Ramos; Panic, Vanja; Morgan, Jeffrey T; Villanueva, Claudio J; Sanchez, Alejandro; Rutter, Jared; Lodhi, Irfan J; Cox, James E; Fisher-Wellman, Kelsey H; Chaudhuri, Dipayan; Gerhart-Hines, Zachary; Funai, Katsuhiko. Mitochondrial phosphatidylethanolamine modulates UCP1 to promote brown adipose thermogenesis. *Science Advances* **9**, 7864 (2023).

31. Kartsoli, S., Kostara, C.E., Tsimihodimos, V., Bbairaktari, E.T. & Christodoulou, D.K. Lipidomics in non-alcoholic fatty liver disease. *World Journal of Hepatology* **12**, 436-450 (2020).

32. Ehud Zigmond, C.V. Two Roads Diverge in the Sick Liver, Monocytes Travel Both. *Cell Press* **10**, 1016 (2020).

33. Zahao, X.-A.C., Guang-Mei; Liu, Yong; Chen, Yu-Xin; Wu, Hong-Yan; Chen, Jin; Xiong, Ya-Li; Tian, Chen; Wang, Gui-Yang; Jia, Bei; Xia, Juan; Wang, Jian; Yan, Xiao-Min; Zhang, Zhao-Ping; Huang, Rui; Wu, Chao. Inhibitory effect of silymarin on CCl4-induced liver fibrosis by reducing Ly6Chi monocytes infiltration. *International Journal of Clinical & Experimental Pathology* **10**, 11941-11951 (2017).

34. Daemen, S.G., Anastasiia; Kalugotla, Gowri; He, Li; Chan, Mandy M.; Beals, Joseph W.: Liss, Kim H.; Klein, Samuel; Feldstein, Ariel E.; Finck, Brian N.; Artyomov, Maxim N.; Schilling, Joel D. Dynamic Shifts in the Composition of Resident and Recruited Macrophages Influence Tissue Remodeling in NASH. *Cell Reports* **34**, 108626 (2021).

35. Liyanage, S.E.G., Peter J.; Ribeiro, Joana; Cristante, Enrico; Sampson, Robert D.; Luhmann, Ulrich F.O.; Ali, Robin R.; Bainbridge, James W. Flow cytometric analysis of inflammatory and resident myeloid populations in mouse ocular inflammatory models. *Experimental Eye Research* **151**, 160-170 (2016).

36. Fry, M. & Green, D.E. Cardiolipin requirement for electron transfer in complex I and III of the mitochondrial respiratory chain. *Journal of Biological Chemistry* **256**, 1874-1880 (1981).

37. Paradies, G., Petrosillo, G., Pistolese, M. & Ruggiero, F.M. Reactive oxygen species affect mitochondrial electron transport complex I activity through oxidative cardiolipin damage. *Gene* **286**, 135-141 (2002).

38. Lange, C., Nett, J.H., Trumpower, B.L. & Hunte, C. Specific roles of protein–phospholipid interactions in the yeast cytochrome bc1 complex structure. *The EMBO Journal* **20**, 6591-6600 (2001).

39. Robinson, N.C. Functional binding of cardiolipin to cytochrome c oxidase. *Journal of Bioenergetics and Biomembranes* **25**, 153-163 (1993).

40. Koliaki, C.*, et al.* Adaptation of hepatic mitochondrial function in humans with non-alcoholic fatty liver is lost in steatohepatitis. *Cell Metab* **21**, 739-746 (2015).

41. Siripoksup, P.*, et al.* Sedentary behavior in mice induces metabolic inflexibility by suppressing skeletal muscle pyruvate metabolism. *J Clin Invest* **134**(2024).

42. Drose, S. & Brandt, U. The Mechanism of Mitochondrial Superoxide Production by the Cytochrome bc1 Complex. *Journal of Biological Chemistry* **283**, 21649-21654 (2008).

43. Marra, F. & Svegliati-Baroni, G. Lipotoxity and the gut-liver axis in NASH pathogenesis. *Hepatology* **68**, 280-295 (2018).

44. Buzzetti, E., Pinzani, M. & Tsochatzis, E.A. The multiple-hit pathogenesis of non-alcoholic fatty liver disease (NAFLD). *Metabolism* **65**, 1038-1048 (2016).

45. Turkseven, S.*, et al.* Mitochondria-targeted antioxidant mitoquinone attenuates liver inflammation and fibrosis in cirrhotic rats. *American Physiological Society* **318**, 298-304 (2020).

46. Karakuzu, O.C., Melissa R.; Liu, Yi; Garsin, Danielle A. Amplex Red Assay for Measuring Hydrogen Peroxide Production from Caenorhabditis elegans. *Bio-protocol* **9**, 3409 (2019).

47. Prola, A.B., Jordan; Vandestienne, Aymeline; Piquereau, Jerome; Denis, Raphael GP; Guyot, Stephane; Chauvin, Hadrien; Mourier, Arnaud; Maurer, Marie; Henry, Celine; Khadhraoui, Nahed; Gallerne, Cindy; Molinie, Thibaut; Courtin, Guillaume; Gressette, Melanie; Solgadi, Audrey; Dumont, Florent; Castel, Julien; Ternacle, Julien; Demarquoy, Jean; Malgoyre, Alexandra; Koulmann, Nathalie; Derumeaux, Genevieve; Giraud, Marie-France; Joubert, Frederic; Veksler, Vladimir; Luquet, Serve; Relaix, Frederic; Tiret, Laurent; Pilot-Storck, Fanny. Cardiolipin content controls mitochondrial coupling and energetic efficiency in muscle. *Science Advances* **7**(2021).

48. Mileykovskaya, E. & Dowhan, W. Cardiolipin-Dependent Formation of Mitochondrial Respiratory Supercomplexes. *Chemistry and Physics of Lipids* **179**, 42-48 (2014).

49. Pennington, E.R., Funai, K., Brown, D.A. & Shaikh, S.R. The role of cardiolipin concentration and acyl chain composition on mitochondrial inner membrane molecular organization and function. *Biochimica et Biophysica Acta (BBA) - Molecular and Cell Biology of Lipids* **1864**, 1039-1052 (2019).

50. Arnarez, C., Marrink, S.J. & Periole, X. Molecular mechanism of cardiolipin-mediated assembly of respiratory chain supercomplexes. *Chemical Science* (2016).

51. Bottinger, L.*, et al.* Phosphatidylethanolamine and Cardiolipin Differentially Affect the Stability of Mitochondrial Respiratory Chain Supercomplexes. *Journal of Molecular Biology* **5**, 677-686 (2012).

52. Dornas, W. & Schuppan, D. Mitochondrial oxidative injury: a key player in nonalcoholic fatty liver disease. *Gastrointestinal and Liver Physiology* **319**, G400-G411 (2020).

53. Gomez, B. & Robinson, N.C. Quantitative Determination of Cardiolipin in Mitochondrial Electron Transferring Complexes by Silicic Acid High-Performance Liquid Chromatography. *Analytical Biochemistry* **267**, 212-216 (1999).

54. Brand, M.D. Mitochondrial generation of superoxide and hydrogen peroxide as the source of mitochondrial redox signaling. *Free Radical Biology and Medicine* **100**, 14-31 (2016).

55. Decker, S.T.F., Katsuhiko. Mitochondrial membrane lipids in the regulation of bioenergetic flux. *Cell Metab* **36**, 1963-1978 (2024).

56. Bessone, F., Razori, M.V. & Roma, M.G. Molecular pathways of nonalcoholic fatty liver disease development and progression. *Cell. Mol. Life Sci.* **76**, 99-128 (2019).

57. Ines C. M. Simoes, R.A., Jose Teixeira, Agnieszka Karkucinska-Wieckowska, Adriana Carvalho, Susana P. Pereira, Rui F. Simoes, Sylwia Szymanska, Michal Dabrowski, Justyna Janikiewicz, Agnieszka Dobrzyn, Paulo J. Oliveira, Yaiza Potes, Mariusz R. Wieckowski. The Alterations of Mitochondrial Function during NAFLD Progression-- An Independent Effect of Mitochondrial ROS Production. *International Journal of Molecular Sciences* **22**, 6848 (2021).

58. Simoes, I.C., Fontes, A., Pinton, P., Zischka, H. & Wieckowski, M.R. Mitochondria in non-alcoholic fatty liver disease. *The International Journal of Biochemistry & Cell Biology* **95**, 93-99 (2017).

59. Goncalves, R.L.S., Schlame, M., Bartelt, A.L., Brand, M.D. & Hotamisligil, G.S. Cardiolipin deficiency in Barth syndrome is not associated with increased superoxide/H2O2 production in heart and skeletal muscle mitochondria. *FEBS Letters* **595**, 415-432 (2021).

60. Xu, Y*., et al.* Loss of protein association causes cardiolipin degradation in Barth syndrome. *Nature Chemical Biology* **12**, 641-647 (2016).

61. Simoes, I.C.A., Ricardo; Teixeira, Jose; Karkucinska-Wieckowska, Agnieszka; Carvalho, Adriana; Pereira, Susana P.; Simoes, Rui F.; Szymanska Sylwia; Dabrowski, Michal; Janikiewicz, Justyna; Dobrzyn, Agnieszka; Oliveira, Paulo J.; Potes, Yaiza; Wieckowski, Mariusz R. . The Alterations of Mitochondrial Function during NAFLD Progression-- An Independent Effect of Mitochondrial ROS Production. *International Journal of Molecular Sciences* **22**, 6848 (2021).

62. Bazan, S*., et al.* Cardiolipin-dependent Reconstitution of Respiratory Supercomplexes from Purified Saccharomyces cerevisiae Complexes III and IV*. *Journal of Biological Chemistry* **288**, 401-411 (2013).

63. Miwa, S*., et al.* Carboxylesterase converts Amplex red to resorufin: Implications for mitochondrial H2O2 release assays. *Free Radical Biology and Medicine* **90**(2016).

Acknowledgements

Contributions

Conception: M.J.B., K.F., M.P., S.A.S., and T.S.T. Experimental design: M.J.B., K.F., P.S., F.M.F., Z.G.-H., and W.L.H. Investigation: M.J.B., K.F., G.C., J.A.M., A.M.P., A.D.P., L.W., T.B.B., J.L.S., P.S., Q.J.P., J.M.J., A.P., S.A.P., P.N.M., G.L.H., A.M.M., S.W., E.R.M., K.E.A., L.S.N., R.H.C., and S.T.D. Methodology: J.A.M., Q.J.P., J.M.J., F.M.F., Z.G.-H., A.P., S.A.P., P.N.M., G.L.H., J.L.C., S.M.N., D.S.L., K.H.F.-W., J.E.C., and L.S.N. Resources: F.M.F., Z.G.-H., W.L.H., K.J.E., and S.A.S. Formal analysis: M.J.B., K.F., G.C., J.A.M., A.D.P., L.W., R.H.C., J.L.C., and S.A.P. Writing: M.J.B. and K.F. All authors read and approved the paper.

1161 **Corresponding Author**

1162 Correspondance to Katsuhiko Funai

1163 E-mail: kfunai@health.utah.edu
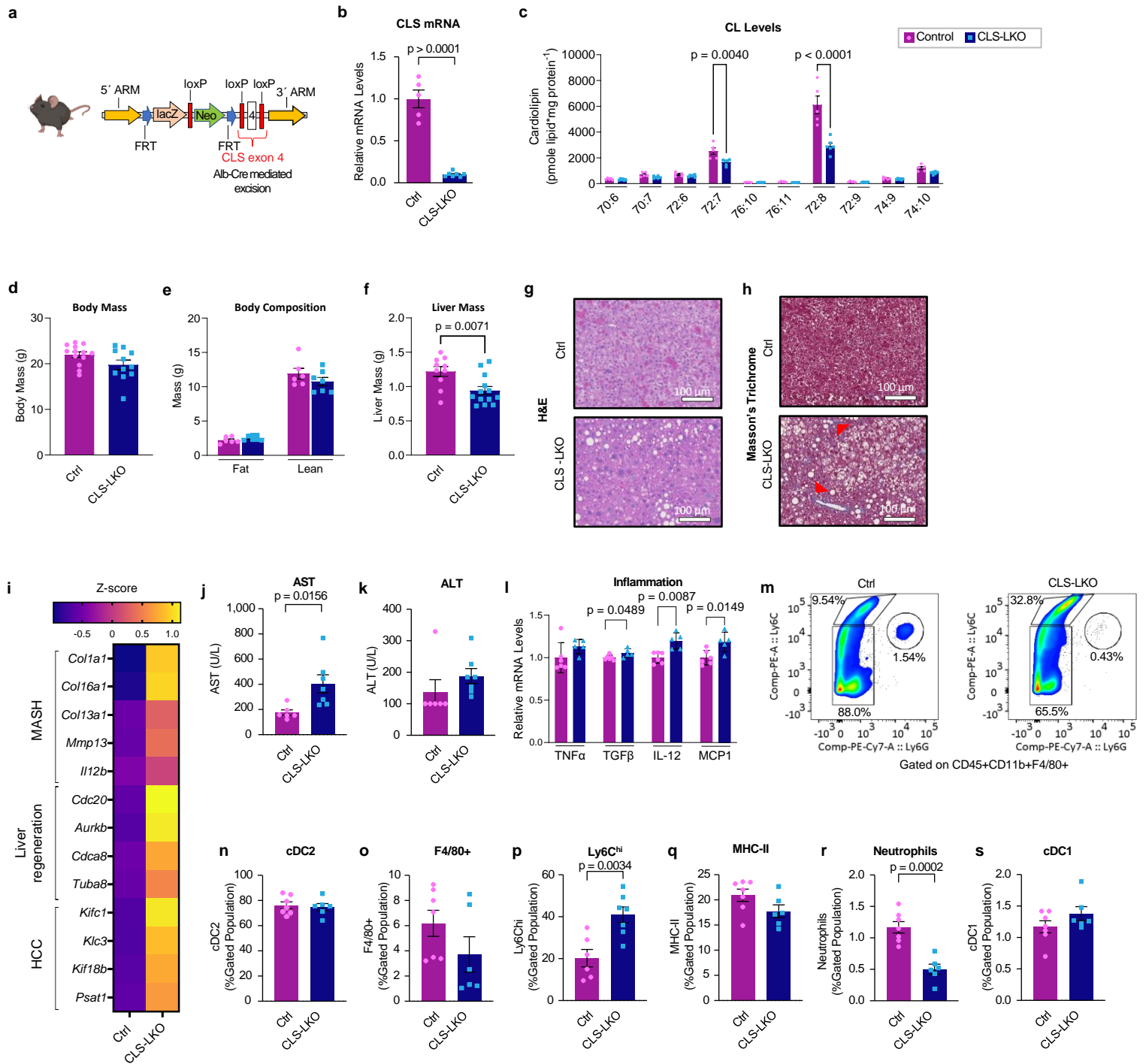
1164

1165 **Ethics Declarations**

1166 Competing Interests

1167 The authors declare no competing interests.

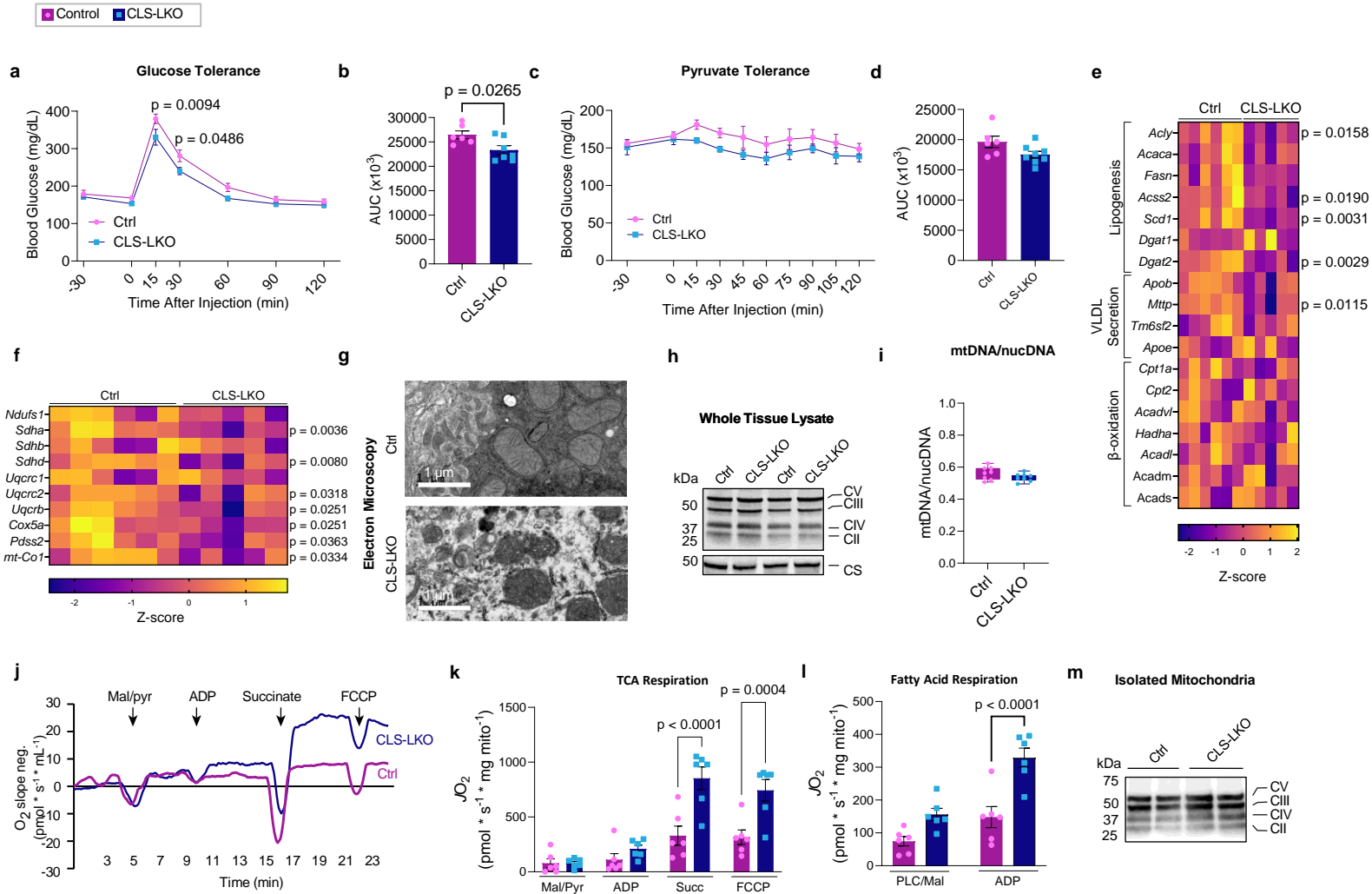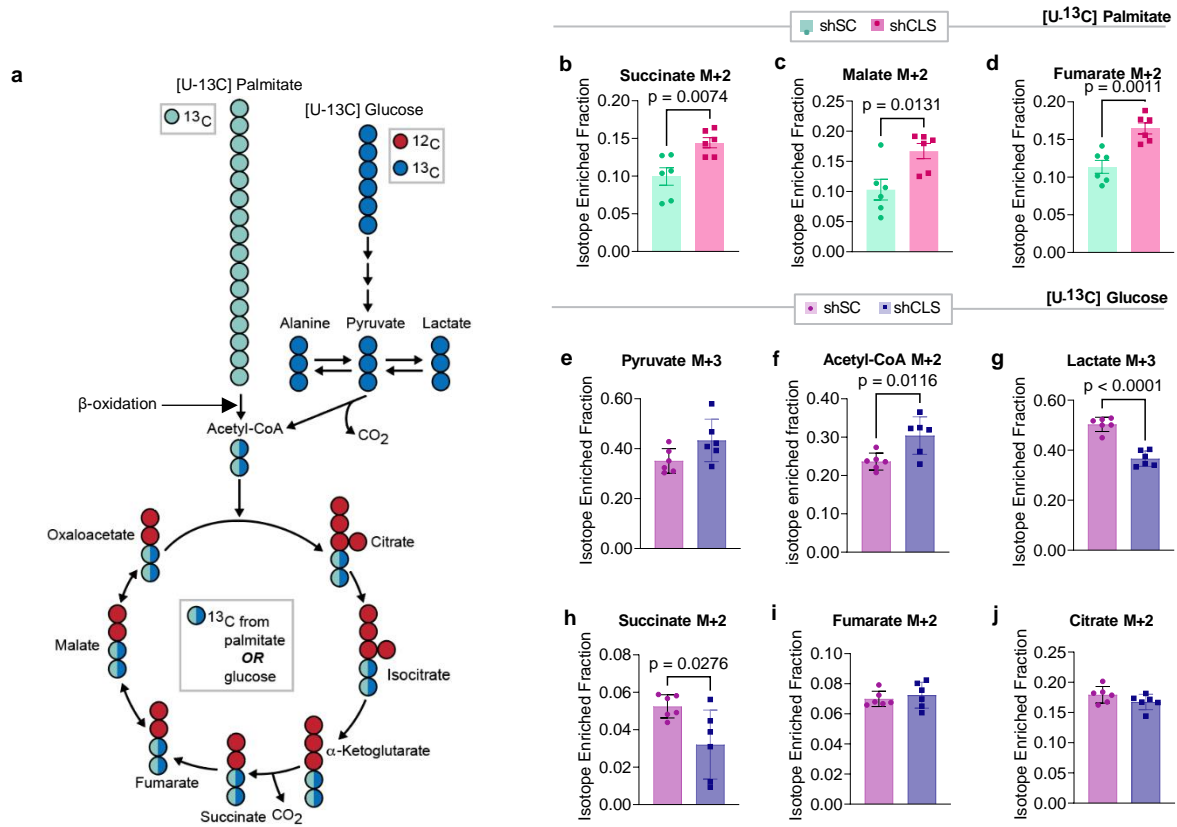**Figure 1.**
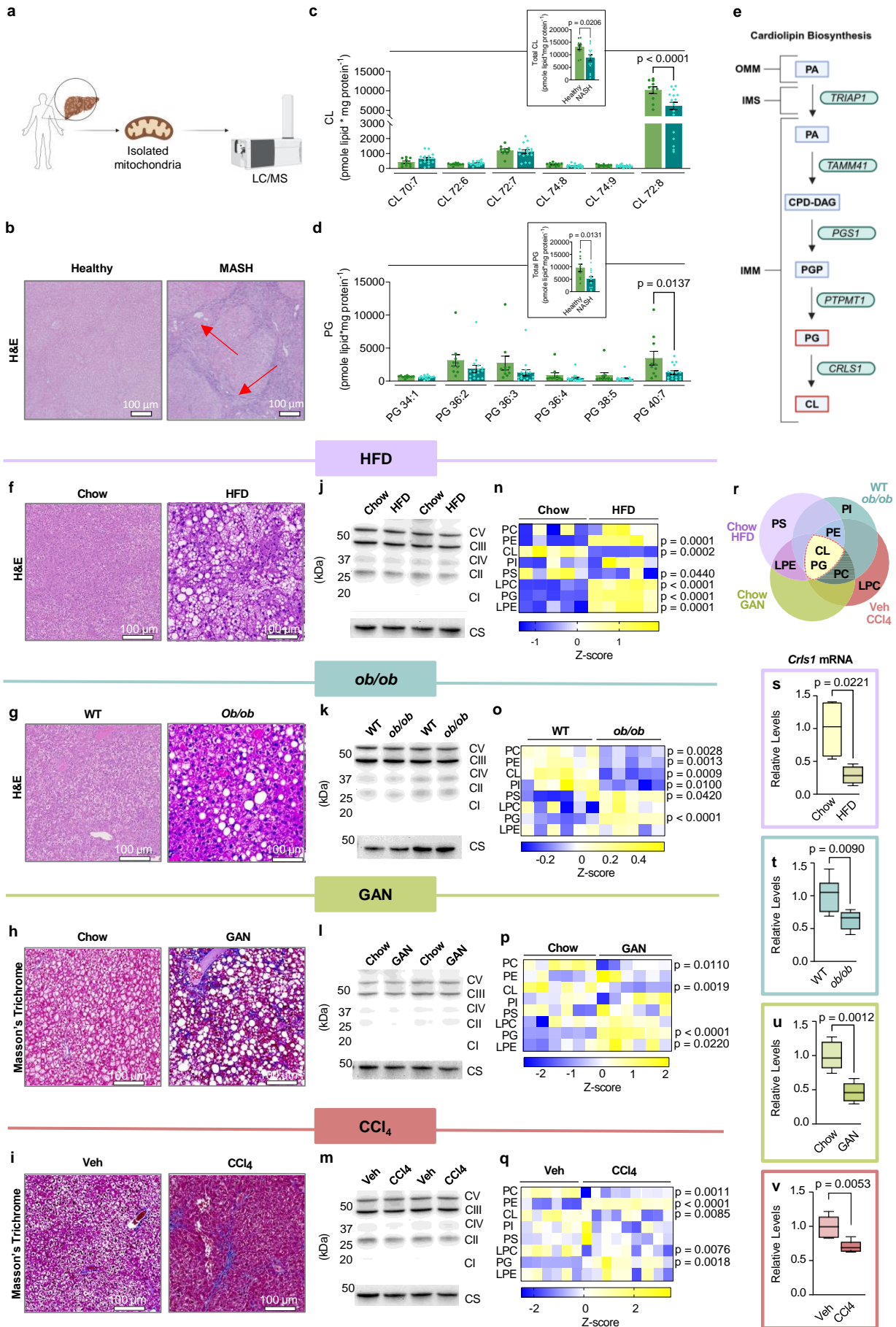
Figure 2.

Figure 3.

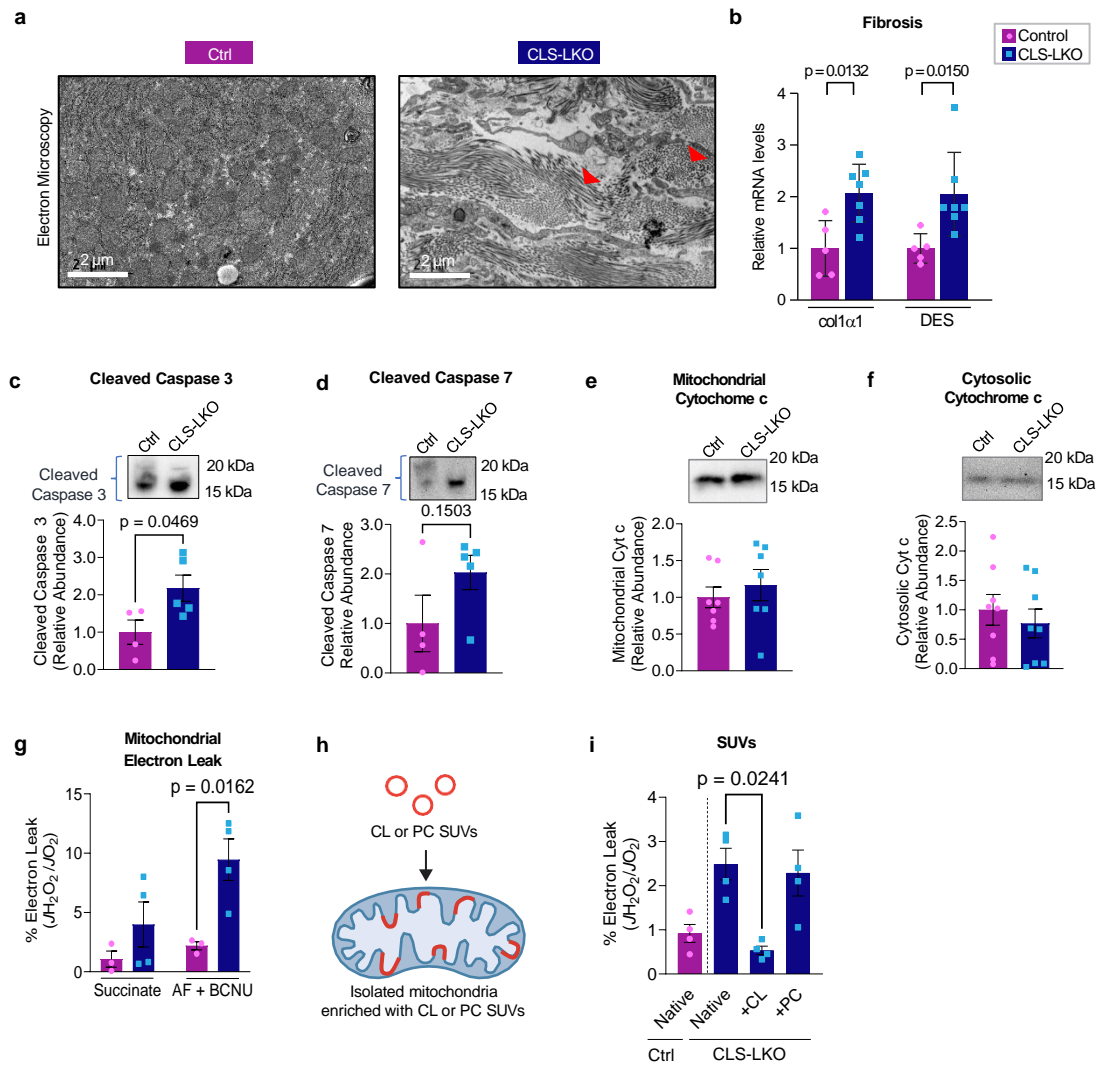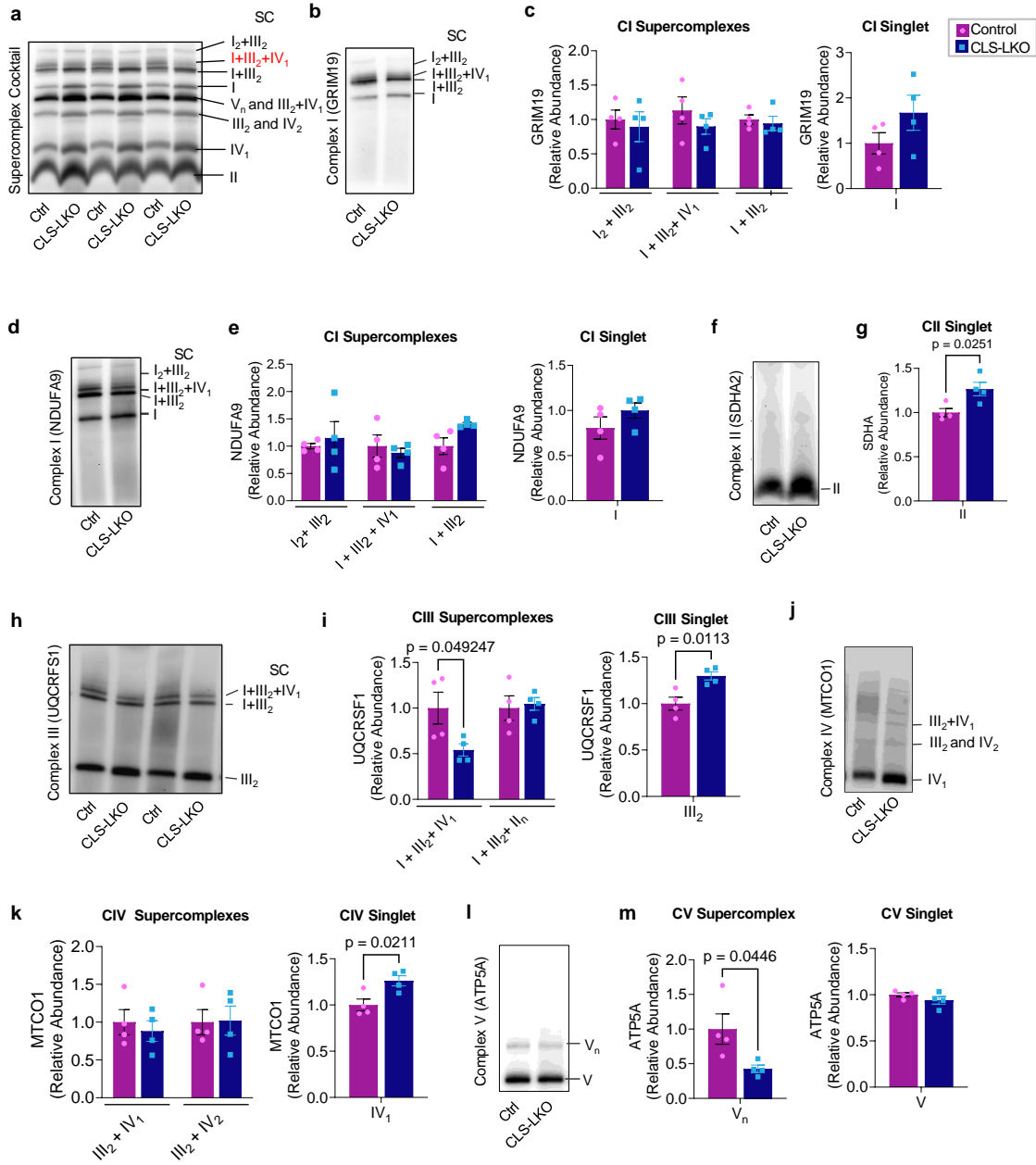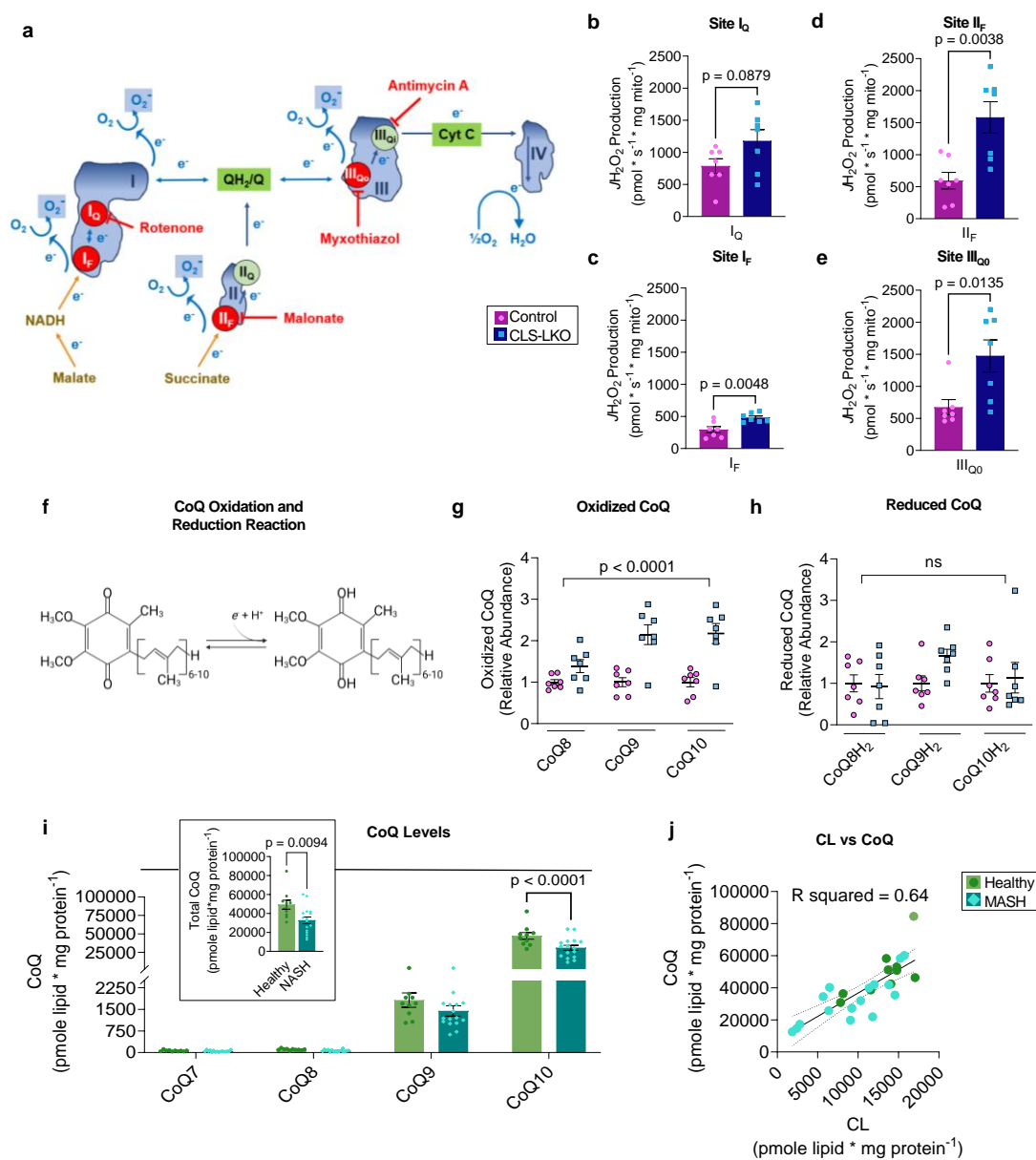**Figure 4.**

Figure 5.

Figure 6.

Figure 7

Extended Data Figure Legends

Extended Data Fig. 1. Mitochondrial phospholipidome from Figure 1j,k.

(a) Abundance of mitochondrial CL in liver of mice fed with standard chow or HFD for 16 wks (n=5 per group). (b) Abundance of mitochondrial PC in liver of mice fed standard chow or HFD for 16 wks (n=5 per group). (c) Abundance of mitochondrial PE in liver of mice fed with standard chow or HFD for 16 wks (n=5 per group). (d) Abundance of mitochondrial PI in liver of mice fed with standard chow or HFD for 16 wks (n=5 per group). (e) Abundance of mitochondrial PS in liver of mice fed with standard chow or HFD for 16 wks (n=5 per group). (f) Abundance of mitochondrial LPC in liver of mice fed with standard chow or HFD for 16 wks (n=5 per group). (g) Abundance of mitochondrial PG in liver of mice fed with standard chow or HFD for 16 wks (n=5 per group). (h) Abundance of mitochondrial LPE in liver of mice fed with standard chow or HFD for 16 wks (n=5 per group). (i) Abundance of mitochondrial CL in liver from wildtype or leptin-deficient mice, 30 wks old (n=6 per group). (j) Abundance of mitochondrial PC in liver from wildtype or leptin-deficient mice, 30 wks old (n=6 per group). (k) Abundance of mitochondrial PE in liver from wildtype or leptin-deficient mice, 30 wks old (n=6 per group). (l) Abundance of mitochondrial PI in liver from wildtype or leptin-deficient mice, 30 wks old (n=6 per group). (m) Abundance of mitochondrial PS in liver from wildtype or leptin-deficient mice, 30 wks old (n=6 per group). (n) Abundance of mitochondrial LPC in liver from wildtype or leptin-deficient mice, 30 wks old (n=6 per group). (o) Abundance of mitochondrial PG in liver from wildtype or leptin-deficient mice, 30 wks old (n=6 per group). (p) Abundance of mitochondrial LPE in liver from wildtype or leptin-deficient mice, 30 wks old (n=6 per group). Statistical significance was determined by 2-way ANOVA with a within-row pairwise comparison. Data represent mean $\pm$ SEM. Measurements taken from a-h were taken from the same samples. Measurements from i-p were taken from the same samples.

Extended Data Fig. 2. Mitochondrial phospholipidome from Figure 1l,m.

(a) Abundance of mitochondrial CL in livers from mice injected with corn oil or carbon tetrachloride for 10 wks (n=5 and 7 per group). (b) Abundance of mitochondrial PC in livers from mice injected with corn oil or carbon tetrachloride for 10 wks (n=5 and 7 per group). (c) Abundance of mitochondrial PE in livers from mice injected with corn oil or carbon tetrachloride for 10 wks (n=5 and 7 per group). (d) Abundance of mitochondrial PI in livers from mice injected with corn oil or carbon tetrachloride for 10 wks (n=5 and 7 per group). (e) Abundance of mitochondrial PS in livers from mice injected with corn oil or carbon tetrachloride for 10 wks (n=5 and 7 per group). (f) Abundance of mitochondrial LPC in livers from mice injected with corn oil or carbon tetrachloride for 10 wks (n=5 and 7 per group). (g) Abundance of mitochondrial PG in livers from mice injected with corn oil or carbon tetrachloride for 10 wks (n=5 and 7 per group). (h) Abundance of mitochondrial LPE in livers from mice injected with corn oil or carbon tetrachloride for 10 wks (n=5 and 7 per group). (i) Abundance of mitochondrial CL in livers from mice fed standard chow or Gubra-Amylin MASH diet for 30 wks (n=6 per group). (j) Abundance of mitochondrial PC in livers from mice fed standard chow or Gubra-Amylin MASH diet for 30 wks (n=6 per group). (k) Abundance of mitochondrial PE in livers from mice fed standard chow or Gubra-Amylin MASH diet for 30 wks (n=6 per group). (l) Abundance of mitochondrial PI in livers from mice fed standard chow or Gubra-Amylin MASH diet for 30 wks (n=6 per group). (m) Abundance of mitochondrial PS in livers from mice fed standard chow or Gubra-Amylin MASH diet for 30 wks (n=6 per group). (n) Abundance of mitochondrial LPC in livers from mice fed standard chow or Gubra-Amylin MASH diet for 30 wks (n=6 per group). (o) Abundance of mitochondrial PG in livers from mice fed standard chow or Gubra-Amylin MASH diet for 30 wks (n=6 per group). (p) Abundance of mitochondrial LPE in livers from mice fed standard chow or Gubra-Amylin MASH diet for 30 wks (n=6 per group). Statistical significance was determined by 2-way ANOVA with a within-row pairwise comparison. Data represent mean $\pm$ SEM. Measurements from a-h were taken from the same samples. Measurements from i-p were taken from the same samples.

Extended Data Fig. 3. Mitochondrial phospholipidome from standard chow or high-fat diet fed control and CLS-LKO livers.

(a) Abundance of mitochondrial PC in liver from control or CLS-LKO mice with standard chow, 8 wks old (*n*=5 and 6 per group). (b) Abundance of mitochondrial PE in liver from control or CLS-LKO mice fed with standard chow, 8 wks old (*n*=5 and 6 per group). (c) Abundance of mitochondrial PI in liver from control or CLS-LKO mice fed with standard chow, 8 wks old (*n*=5 and 6 per group). (d) Abundance of mitochondrial PS in liver from control or CLS-LKO mice fed with standard chow, 8 wks old (*n*=5 and 6 per group). (e) Abundance of mitochondrial LPC in liver from control or CLS-LKO mice fed with standard chow, 8 wks old (*n*=5 and 6 per group). (f) Abundance of mitochondrial PG in liver from control or CLS-LKO mice fed with standard chow, 8 wks old (*n*=5 and 6 per group). (g) Abundance of mitochondrial LPE in liver from control or CLS-LKO mice fed with standard chow, 8 wks old (*n*=5 and 6 per group). (h) Abundance of mitochondrial CL in liver from control or CLS-LKO mice fed a high-fat diet for 8 wks (*n*=11 and 12 per group). (i) Abundance of mitochondrial PC in liver from control or CLS-LKO mice fed a high-fat diet for 8 wks (*n*=11 and 12 per group). (j) Abundance of mitochondrial PE in liver from control or CLS-LKO mice fed a high-fat diet for 8 wks (*n*=11 and 12 per group). (k) Abundance of mitochondrial PI in liver from control or CLS-LKO mice fed a high-fat diet for 8 wks (*n*=11 and 12 per group). (l) Abundance of mitochondrial PS in liver from control or CLS-LKO mice fed a high-fat diet for 8 wks (*n*=11 and 12 per group). (m) Abundance of mitochondrial LPC in liver from control or CLS-LKO mice fed a high fat diet for 8 wks (*n*=11 and 12 per group). (n) Abundance of mitochondrial PG in liver from control or CLS-LKO mice fed a high-fat diet for 8 wks (*n*=11 and 12 per group). (o) Abundance of mitochondrial LPE in liver from control or CLS-LKO mice fed a high fat diet for 8 wks (*n*=11 and 12 per group). Statistical significance was determined by 2-way ANOVA with a within-row pairwise comparison. Data represent mean $\pm$

SEM. Measurements from a-g were taken from the same samples. Measurements from h-o were taken from the same samples.

Extended Data Fig. 4. Additional histological and transcriptomic data from control and CLS-LKO mice.

(a) Representative H&E staining of livers from control and CLS-LKO mice fed a HFD for 8 wks. (b) Representative Masson's Trichrome staining of livers from control and CLS-LKO mice fed a HFD for 8 wks. (c) Volcano plot of differentially expressed genes in livers taken from control and CLS-LKO mice fed with standard chow (n=5 and 7 per group). (d) Pathway analysis of transcriptomic data in livers taken control and CLS-LKO mice fed with standard chow (n=5 and 7 per group). Pathway analysis was performed using the Reactome Pathway Database. Measurements from a and b were taken from distinct samples. Measurements from c and d were taken from the same samples.

Extended Data Fig. 5. Additional metabolic, mitochondrial, and fluxomic phenotyping data with CLS deletion.

(a) mRNA levels of lipogenic genes in livers from control and CLS-LKO mice fed with standard chow (n=6 and 7 per group). (b) Serum triglycerides for control and CLS-LKO mice fed with standard chow (n=6 and 7 per group). (c) JO_2 consumption in isolated liver mitochondria from control or CLS-LKO mice fed a HFD for 8 wks in response to 0.5 mM malate, 5 mM pyruvate, 2.5 mM ADP, 10 mM succinate, and 1.5 µM FCCP (n=11 and 12 per group). (d) JO_2 consumption in isolated liver mitochondria from control or CLS-LKO mice fed a HFD for 8 wks in response to 0.02 mM palmitoyl-carnitine, 0.5 mM malate, and 2.5 mM ADP (n=7 per group). (e) Levels of labeled glycine from glucose tracing in hepa1-6 cells without (shSC) or with CLS deletion (shSLC) (n=6 per group). (f) Levels of labeled aspartate from glucose tracing in hepa1-6 cells without (shSC) or with CLS deletion (shSLC) (n=6 per group). (g) Levels of labeled 3-

phosphoglyceric acid from glucose tracing in hepa1-6 cells without (shSC) or with CLS deletion (shSLC) (n=6 per group). (h) Levels of labeled alanine from glucose tracing in hepa1-6 cells without (shSC) or with CLS deletion (shSLC) (n=6 per group). (i) Levels of labeled malate from glucose tracing in hepa1-6 cells without (shSC) or with CLS deletion (shSLC) (n=6 per group). Statistical significance was determined by 2-way ANOVA with a within-row pairwise comparison (a, c, and d) and unpaired Student's T test (b, and e-i). Data represent mean $\pm$ SEM. Measurements from a and b were taken from distinct samples. Measurements from c and d were taken from the same samples. Measurements from e-i were taken from the same samples.

Extended Data Fig. 6. Additional mitochondrial phenotyping data with CLS deletion.

(a) Levels of mitochondrial cytochrome c in livers of control and CLS-LKO mice fed a HFD for 8 wks (n=6 per group). (b) Levels of cytosolic cytochrome c in livers of control and CLS-LKO mice fed a HFD for 8 wks (n=6 per group). (c) H_2O_2 emission and production in isolated liver mitochondria from control or CLS-LKO mice fed a HFD for 8 wks, stimulated with succinate, or succinate and auranofin and BCNU (n=9 and 8 per group). (d) H_2O_2 emission and production in isolated liver mitochondria from hepa1-6 cells without (shSC) or with CLS deletion (shSLC), stimulated with succinate, or succinate and auranofin and BCNU (n=3 per group). (e) Electron leak of liver mitochondria from control mice fused with SUVs (n=4 per group). Statistical significance was determined by 2-way ANOVA with a within-row pairwise comparison (c, d, and e) and unpaired Student's T test (a and b). Measurements from a and b were taken from the same samples. Measurements from c, d, and e were taken from distinct samples.

Extended Data Fig. 7. Additional data on coenzyme Q

(a) Total CoQ_8 levels in whole liver tissue from control and CLS-LKO mice (n=7 per group). (b) Total CoQ_9 levels in whole liver tissue from control and CLS-LKO mice (n=7 per group). (c) Total CoQ_{10} levels in whole liver tissue from control and CLS-LKO mice (n=7 per group). (d)

Oxidized CoQ_8 levels in whole liver tissue from control and CLS-LKO mice (n=7 per group). (e) Reduced CoQ_8 levels in whole liver tissue from control and CLS-LKO mice (n=7 per group). (f) Oxidized CoQ_9 levels in whole liver tissue from control and CLS-LKO mice (n=7 per group). (g) Reduced CoQ_9 levels in whole liver tissue from control and CLS-LKO mice (n=7 per group). (h) Oxidized CoQ_{10} levels in whole liver tissue from control and CLS-LKO mice (n=7 per group). (i) Reduced CoQ_{10} levels in whole liver tissue from control and CLS-LKO mice (n=7 per group). (j) Oxidized CoQ_8 levels in isolated mitochondria from control and CLS-LKO mice (n=7 per group). (k) Reduced CoQ_8 levels in isolated mitochondria from control and CLS-LKO mice (n=7 per group). (l) Oxidized CoQ_9 levels in isolated mitochondria from control and CLS-LKO mice (n=7 per group). (m) Reduced CoQ_9 levels in isolated mitochondria from control and CLS-LKO mice (n=7 per group). (n) Oxidized CoQ_{10} levels in isolated mitochondria from control and CLS-LKO mice (n=7 per group). (o) Reduced CoQ_{10} levels in isolated mitochondria from control and CLS-LKO mice (n=7 per group). Statistical significance was determined by unpaired Student's T test. Data represent mean $\pm$ SEM. Measurements from a-c were taken from the same samples. Measurements from d-i and j-o were taken from the same samples.
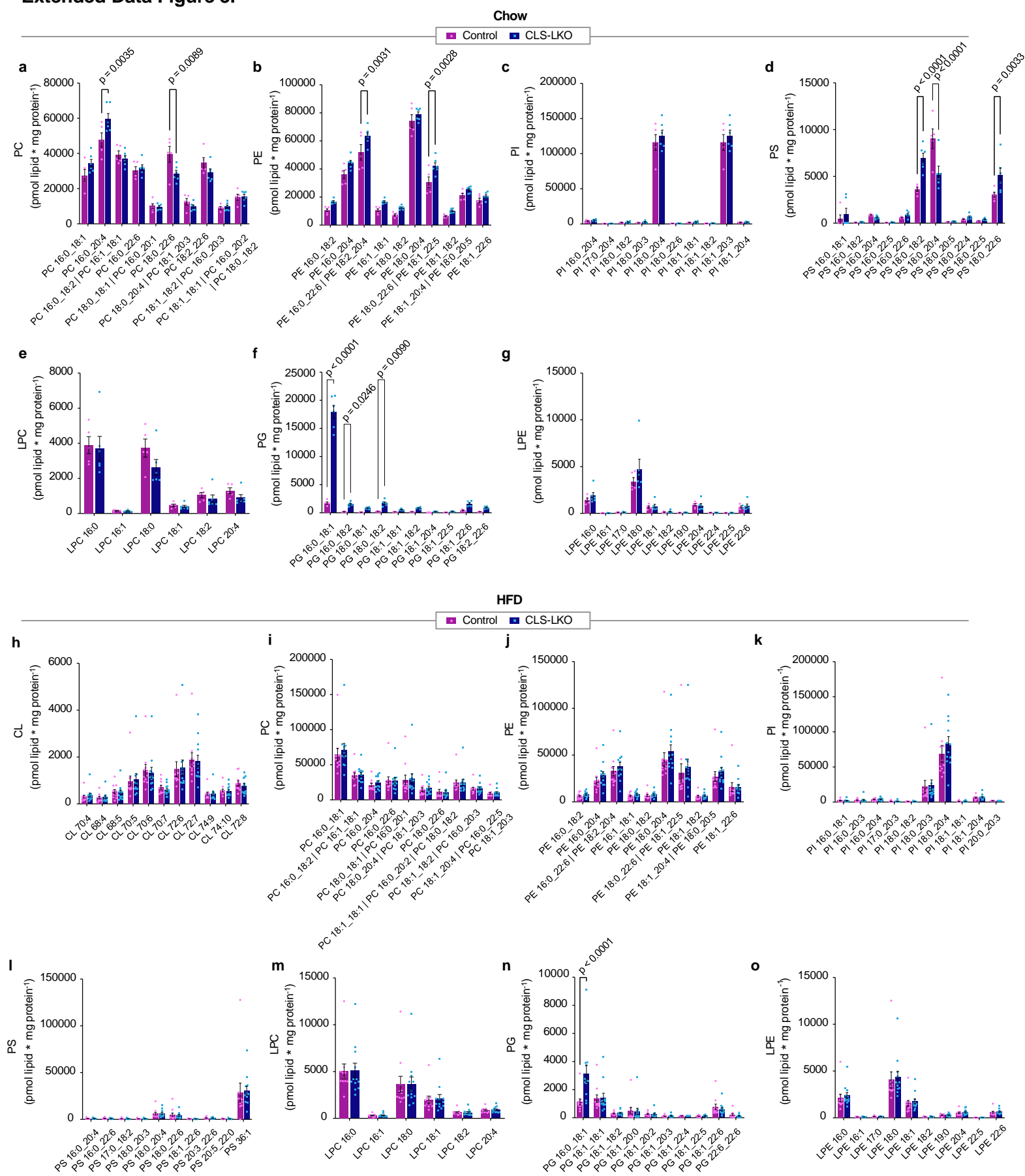
Extended Data Figure 1.
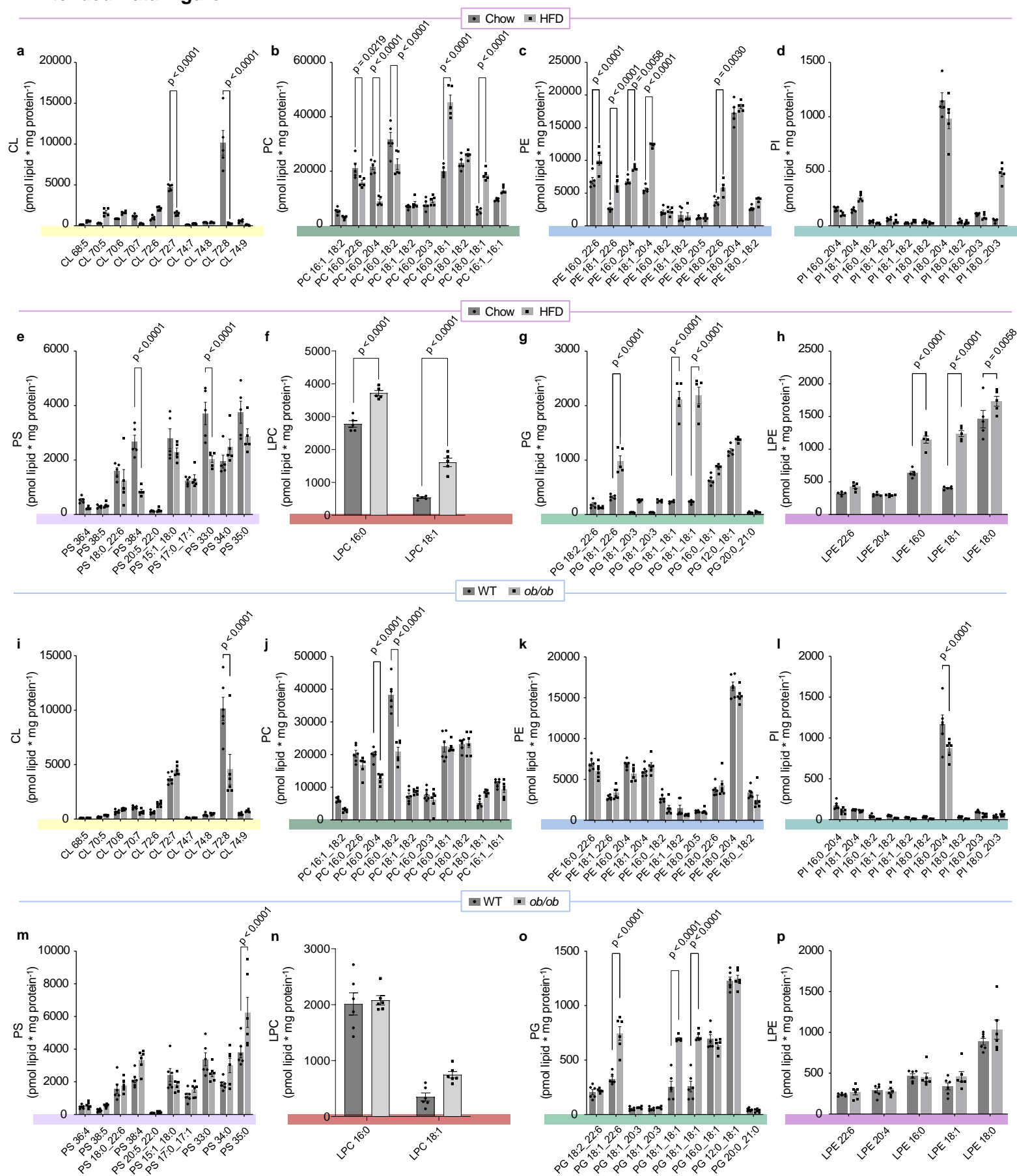
Extended Data Figure 2.
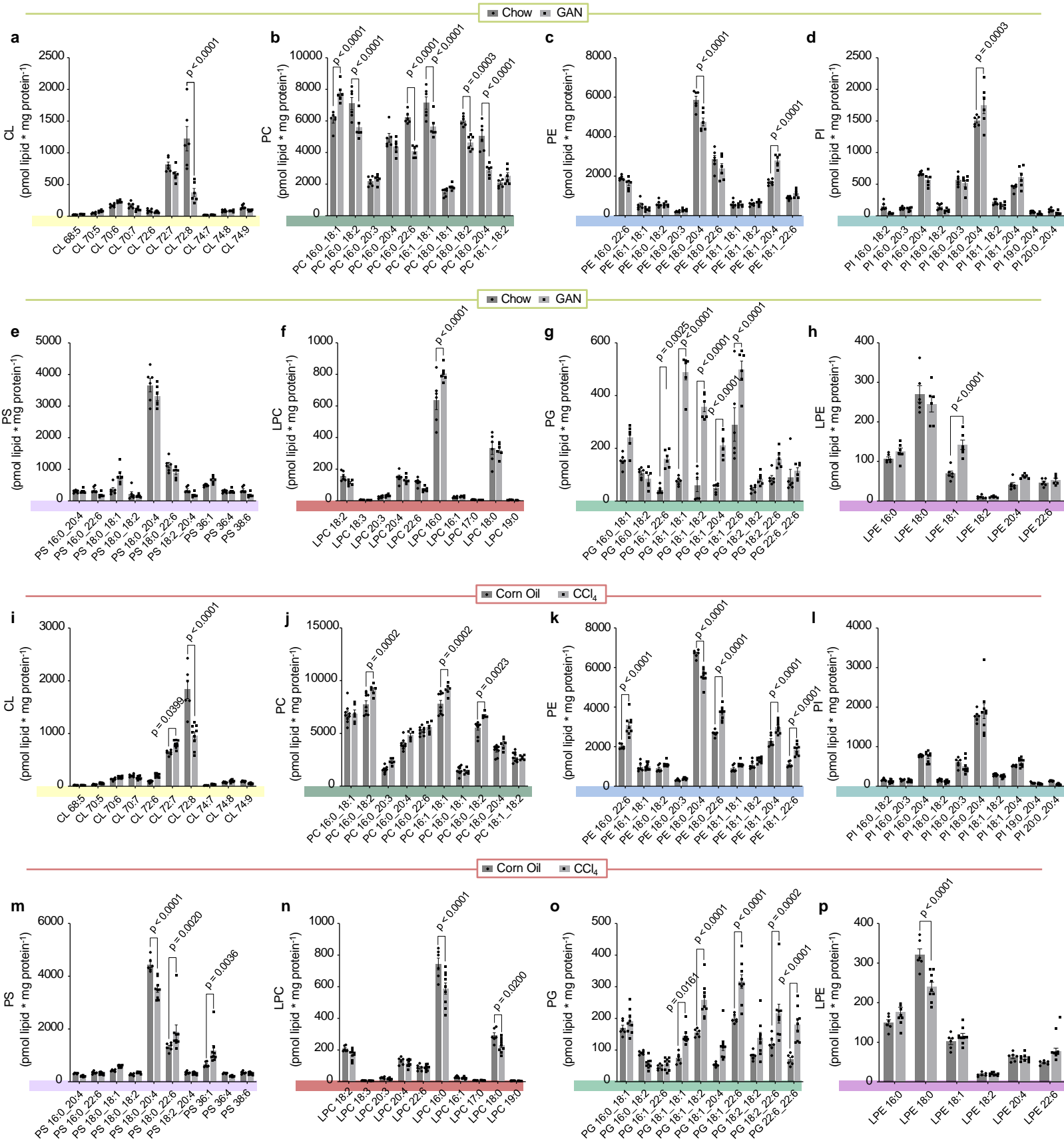
Extended Data Figure 3.

Extended Data Figure 4.
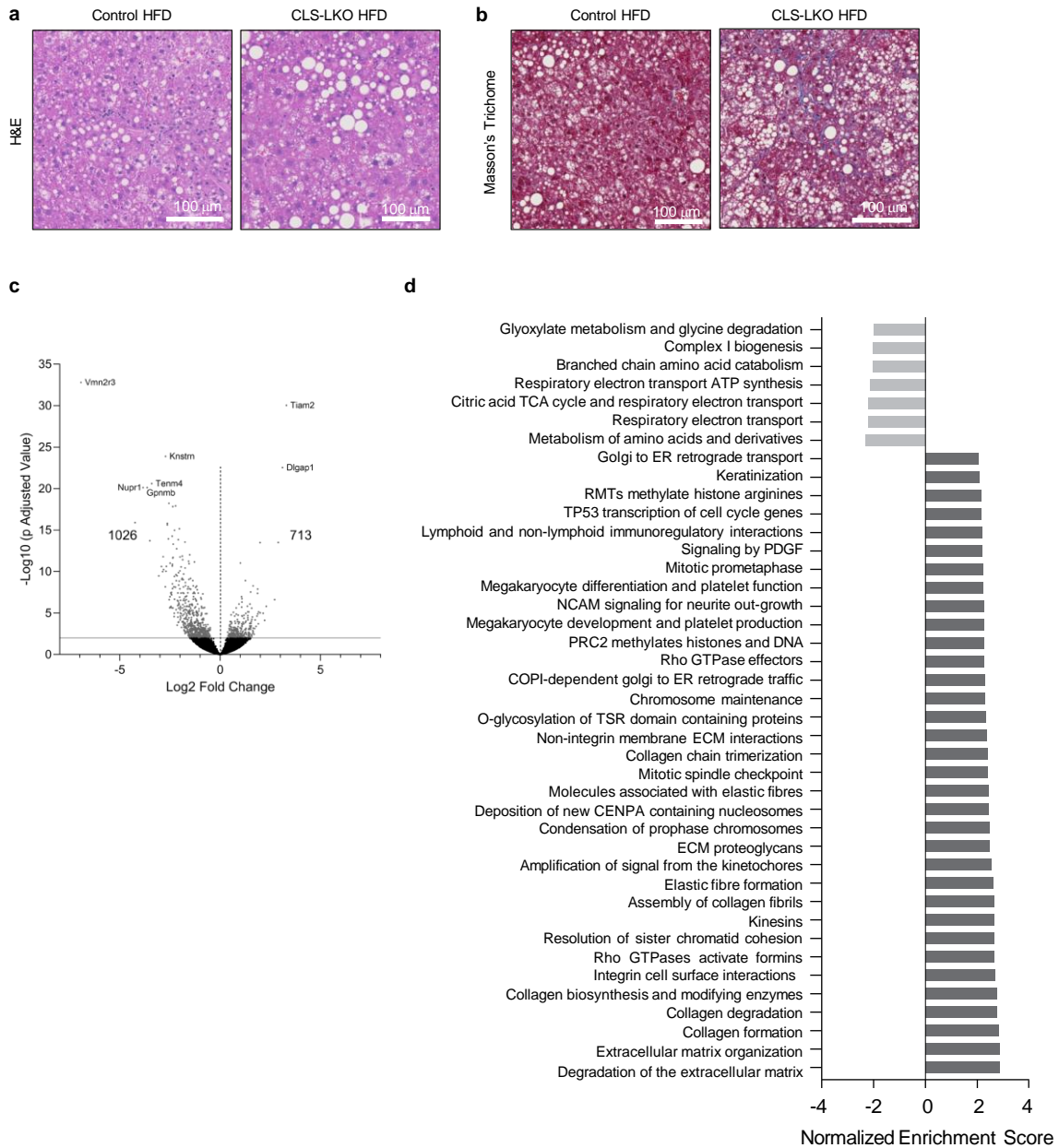
Extended Data Figure 5.
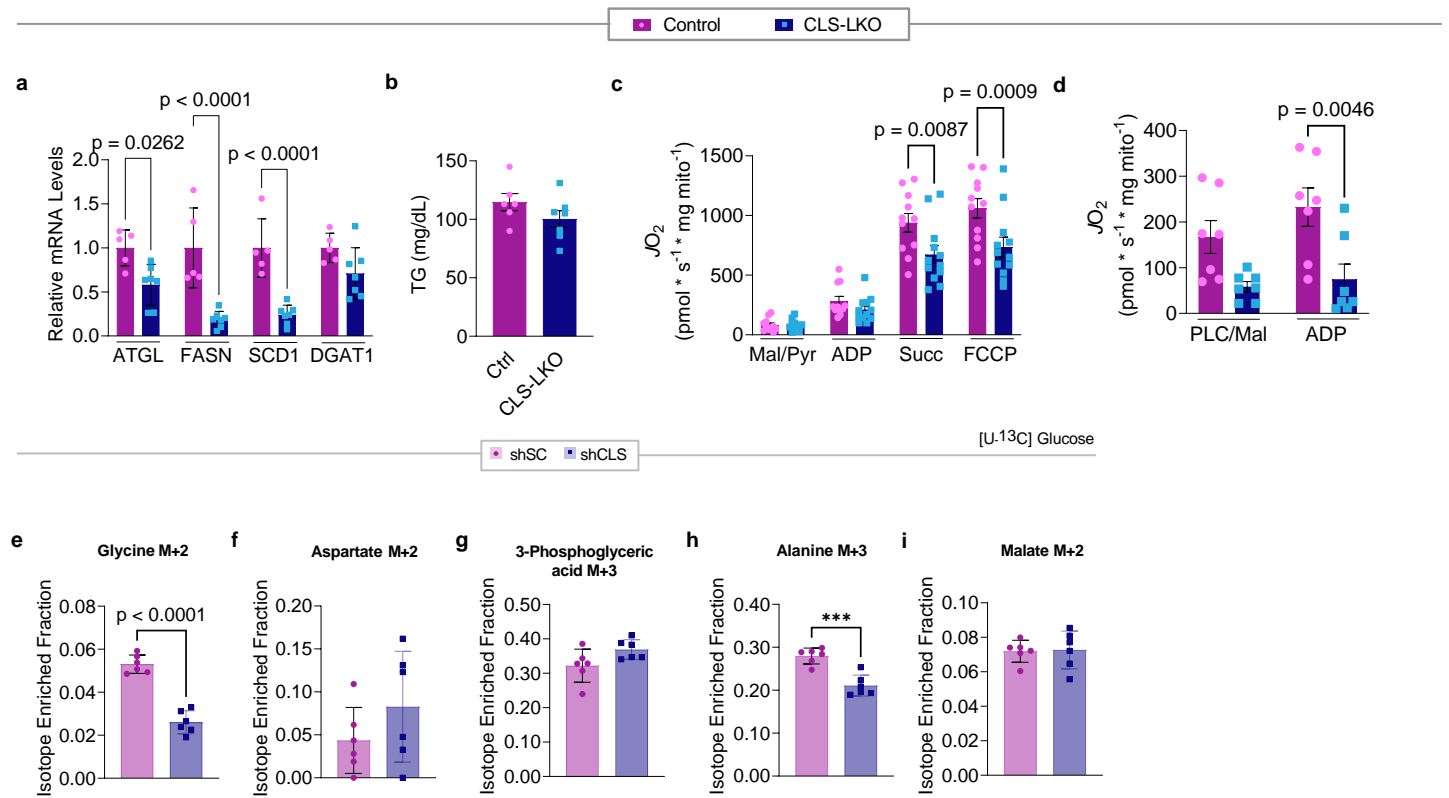
Extended Data Figure 6.
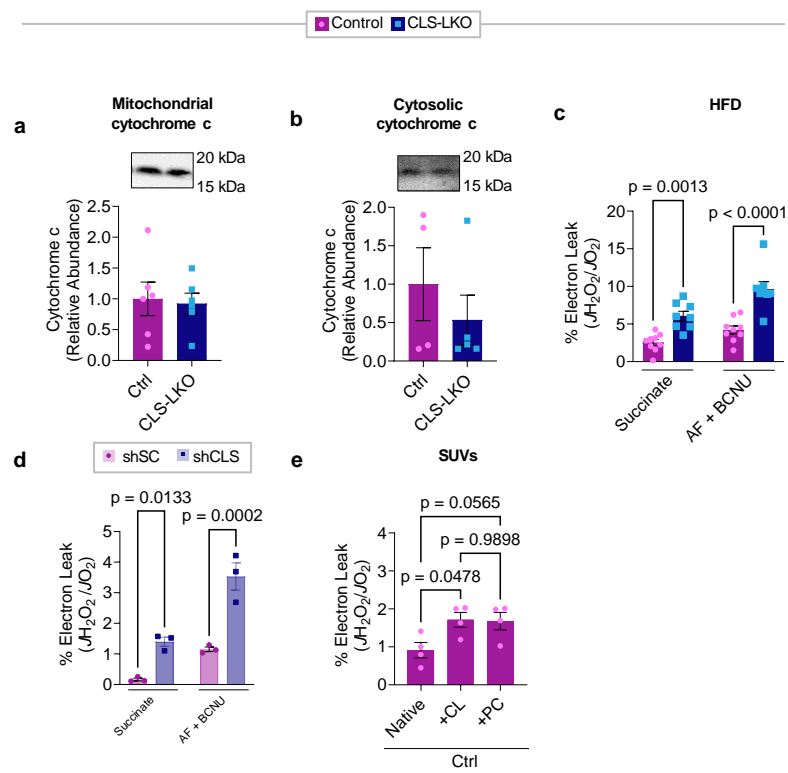
Extended Data Figure 7.
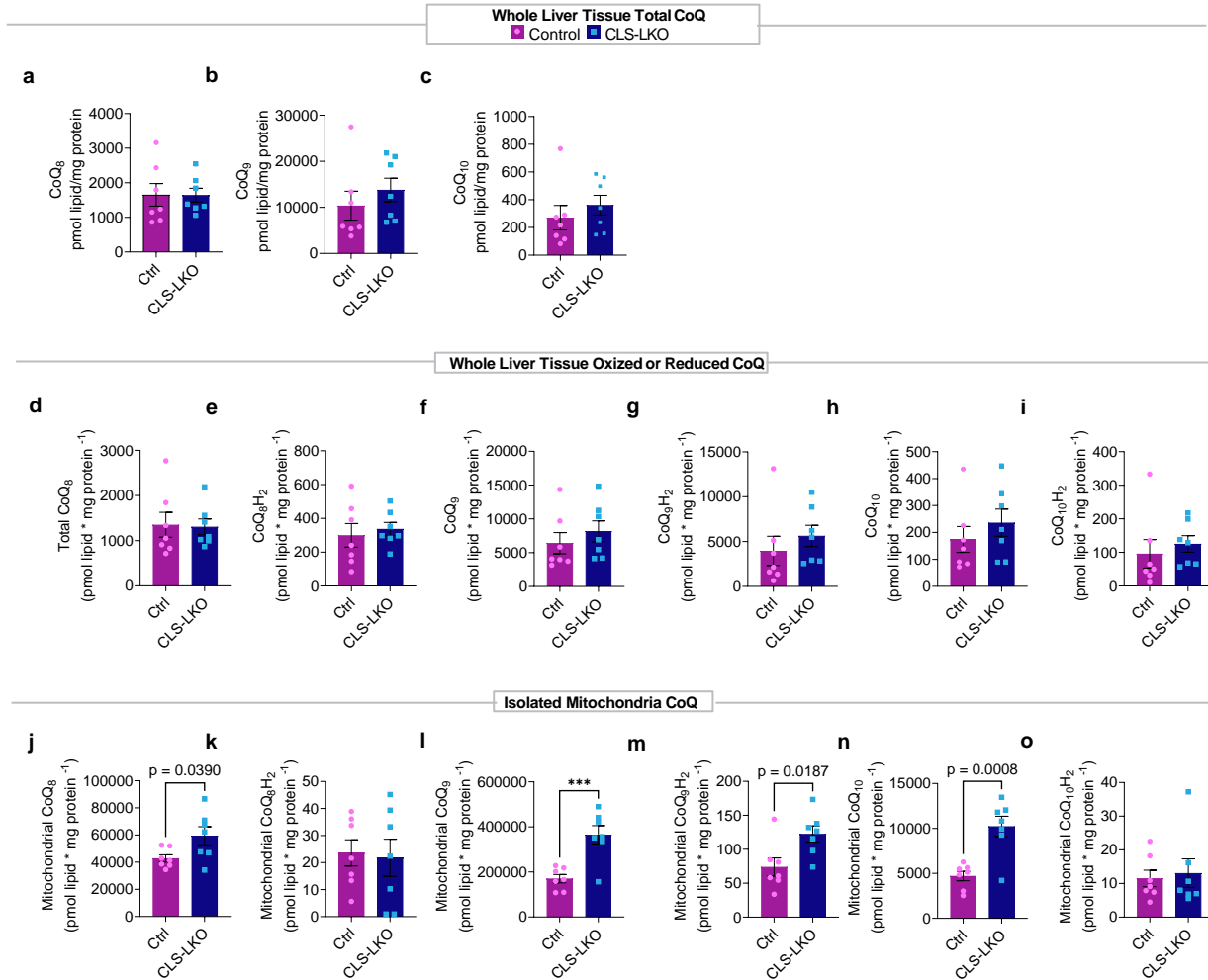
Extended Data Table 1.

Patient demographic information

	Healthy	MASH
Age at time of collection	50.3 ± 9.6 yrs	62.2 ± 7.1 yrs
Sex	Male: 1 Female: 10	Male: 9 Female: 8
Alcohol use?	N/A	Yes: 0 No: 17
Race	White: 9 African American: 1 Asian: 1	White: 10 Unknown: 7

Extended Data Table 2.

Reagents and resources

REAGENT or RESOURCE	SOURCE	IDENTIFIER
Antibodies		
GRIM19	Abcam	ab110240
SDHA	Abcam	ab14715
UQCRFS1	Abcam	ab14746
MTCO1	Abcam	ab14705
ATP5a	Abcam	Ab14748
NDUFA9	Abcam	Ab14713
Total OxPhos Antibody cocktail	Abcam	MS604-300
Citrate Synthetase	Abcam	Ab96600
Cytochrome c	Cell Signaling	11940S
Caspase-3	Cell Signaling	9661S
Caspase-7	Cell Signaling	9491S
CD16/32 (Fc Block, clone 93)	Biolegend	101308
CD45 (FITC, clone S18009F)	Biolegend	157214
CD11b (BVC421, clone M1/70)	Biolegend	101202
F4/80 (APC, clone BM8)	Biolegend	123102
TIM4 (PerCP/Cy5.5, clone RMT4-54)	Biolegend	130020
Ly6C (PE, clone HK1.4)	Biolegend	128008
MHCII (BV605, clone M5/114.15.2)	Biolegend	107639
CD11c (BV785, clone N418)	Biolegend	117302
Ly6G (PE/Cy7, clone 1A8)	Biolegend	164504
OxPhos Blue Native WB Antibody Cocktail	ThermoFisher	45-7999
Bacterial and virus strains		
Second-generation lentiviral-mediated knockdown system		
NEB Stable Competent E. Coli	NEB	C3040H
Biological samples		
Chemicals, peptides, and recombinant proteins		
Amplex Red Reagent	ThermoFisher Scientific	A12222
Auranofin	Sigma Aldrich	A6733
Carmustine (BCNU)	Sigma Aldrich	C0400
SPLASH Mix	Avanti Polar Lipids	330707
Cardiolipin Mix I	Avanti Polar Lipids	LM6003
Bovine Serum Albumin	Sigma Aldrich	A7030

Protease Inhibitor Cocktail	Thermo Scientific	78446
Tamoxifen	Sigma Aldrich	T5648
Sunflower Oil	Sigma Aldrich	S5007
TRIzol	Thermo Scientific	15596018
Mini-PROTEAN TGX Gels	BioRad	4561086
ECL	PerkinElmer	104001EA
Malate	Sigma Aldrich	M7397
Pyruvate	Sigma Aldrich	P2256
GDP	Sigma Aldrich	G7127
CL 316,243 hydrate	Sigma Aldrich	C5976
ADP	Sigma Aldrich	A5285
ATP	Sigma Aldrich	A9187
Glutamate	Sigma Aldrich	G5889
Succinate	Sigma Aldrich	S3674
Carnitine	Sigma Aldrich	8.40092
Palmitoyl-CoA	Sigma Aldrich	P9716
Palmitoyl-L-carnitine	Sigma Aldrich	P1645
SYBR Green	Thermo Scientific	A25776
4% Paraformaldehyde	Thermo	J19943-K2
Opti-MEM	Gibco	31985
DMEM	Gibco	1195-092
FBS	Gibco	10082-147
Penicillin-streptomycin	Gibco	15140122
CL for SUVs	Avanti Polar Lipids	840012
PC for SUVs	Avanti Polar Lipids	850375C
PAGE 3-12% Bis-Tris Gels	Thermo Scientific	BN1001BOX
NativePage 20x Cathode Buffer	Invitrogen	BN2002
NativePage 5% G-250 Sample additive	Invitrogen	BN2004
Nativepage 4x Sample Buffer	Invitrogen	BN2003
CoQ Standard	Cambridge Isotope Labs	CIL DLM-10279
Palmitic acid (U-$^{13}C_{16}$)	Cambridge Isotope Labs	CLM-409-0.1
D-Glucose ((U-$^{13}C_{6}$)	Cambridge Isotope Labs	CLM-1396-5
Critical commercial assays		
Pierce BCA Protein Assay Kit	Thermo Scientific	23227
iScript cDNA Synthesis Kit	BioRad	1708891
SDH Detection Assay Kit	Abcam	ab228560
Direct-zol RNA Miniprep Plus Kit	Zymo	R2070
DNeasy Blood and Tissue Kit	Qiagen	69504

Deposited data		
Experimental models: Cell lines		
HEK293T cells	ATCC	CTRL-3216
Hepa 1-6 murine hepatoma cells	ATCC	CRL-1830
Experimental models: Organisms/strains		
Mouse: CLS conditional knockout (CLS-cKO)	Sustarsic et al. 2018	N/A
Mouse: CLS-LKO	This paper	N/A
Mouse: Alb-Cre	Jackson Laboratory	003574
Oligonucleotides		
RT qPCR Primer ATGL F (CCACTCACATCTACGGAGCC)	www.IDTDNA.com	
RT qPCR Primer ATGL R (TAATGTTGGCACCTGCTTCA)	www.IDTDNA.com	
RT qPCR Primer DGAT1 F (GACGGCTACTGGGATCTGA)	www.IDTDNA.com	
RT qPCR Primer DGAT1 R (TCACAACACACCAATTCAGG)	www.IDTDNA.com	
RT qPCR Primer FAS F (GGATAGCTGTGTAGTGTAACCAT)	www.IDTDNA.com	
RT qPCR Primer FAS R (GGTCATCGTGATAACCACACA)	www.IDTDNA.com	
RT qPCR Primer SCD1 F (GCTCTACACCTGCCTCTTCG)	www.IDTDNA.com	
RT qPCR Primer SCD1 R (CAGCCGAGCCTTGTAAGTTC)	www.IDTDNA.com	
RT qPCR Primer CLS F (TGACCTATGCAGATCTTATTCCA)	Johnson et al. 2019	
RT qPCR Primer CLS R (TGGCAGAGTTCGGTATCTGA)	Johnson et al. 2019	
RT qPCR Primer TNFa F (CCACCACGCTCTTCTGTCTAC)	www.IDTDNA.com	
RT qPCR Primer TNFa R (AGGGTCTGGGCCATAGAACT)	www.IDTDNA.com	
RT qPCR Primer Taz F (CCCTCCATGTGAAGTGGCCATTCC)	Johnson et al. 2019	
RT qPCR Primer Taz R (TGGTGGTTGGAGACGGTGATAAGG)	Johnson et al. 2019	
mtDNA F: (TTAAGACACCTTGCCTAGCCACAC)	Mouse Primer Depot NCI/NIH	
mtDNA R: (CGGTGGCTGGCACGAAATT)	Mouse Primer Depot NCI/NIH	

nucDNA F: (ATGACGATATCGCTGCGCTG)	Mouse Primer Depot NCI/NIH	
nucDNA R: (TCACTTACCTGGTGCCTAGGGC)	Mouse Primer Depot NCI/NIH	
Recombinant DNA		
Sc	Addgene	1864
Crls1	Sigma Aldrich	TRCN0000123937
psPAX2	Addgene	12260
pMD2.G	Addgene	12259
Software and algorithms		
GraphPad Prism 9.0	GraphPad	N/A
Other		